Marine and Petroleum Geology 170 (2024) 107090

Contents lists available at ScienceDirect

Marine and Petroleum Geology

journal homepage: www.elsevier.com/locate/marpetgeo

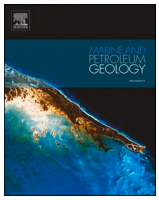

# Evaluation of fluid mobility and factors influencing the deep tight sandstone of the third member of the Shahejie formation in the Jiyang depression, Bohai Bay Basin

Yuchao Wang [a,b], Dongxia Chen [a,b,*], Lanxi Rong [a,b], Jialing Chen [a,b], Fuwei Wang [a,b], Shijie He [a,b], Yuqi Wang [a,b], Zijie Yang [a,b], Wenzhi Lei [a,b]

[a] State Key Laboratory of Petroleum Resources and Engineering, China University of Petroleum (Beijing), Beijing,102249, China
[b] College of Geosciences, China University of Petroleum (Beijing), Beijing, 102249, China

ARTICLE INFO

*Keywords:*
Bohai Bay basin
Tight sandstone
Nuclear magnetic resonance
Pore structure
Movable fluid
Lower limit of the movable pore radius

ABSTRACT

The Paleogene lacustrine delta–turbidite facies sandstones of the Third Member of the Shahejie Formation ($Es_3$) in the Linnan Depression have abundant tight oil resources. Movable fluids can independently characterize reservoir fluid mobility and recovery efficiency, which are essential for accurate reservoir assessment and efficient development and evaluation of oil reservoirs. Systematic research on the distribution patterns and controlling factors of movable fluids in the tight sandstone reservoirs of the Linnan Depression is lacking. To address this gap, this study employs multi-gradient centrifugation combined with Nuclear Magnetic Resonance (NMR) to characterize fluid mobility and determine the lower limit of the movable fluid pore radius (LLMPR) in various lithofacies of lacustrine delta-turbidite facies sandstones. In conjunction with core descriptions, thin section observations, X-ray diffraction (XRD) analysis, gas permeability tests, and High-pressure mercury injection (HPMI) data, this research explicates the macroscopic impacts of depositional and diagenetic processes and the microscopic effects of pore structure on fluid movability. The study identifies four lithofacies (delta front facies massive siltstone (DFMS)、delta front facies laminated siltstone (DFLS)、slump turbidite facies siltstone (STS), and slump turbidite facies calcareous siltstone (STCS)) with corresponding pore structures and space types (I-micropores, II-micropores, mesopores, macropores). DFLS and DFMS feature well-developed primary intergranular and intragranular dissolution pores, high HPMI mercury intrusion saturation, and large average pore radius, primarily contributing to fluid mobility through mesopores and macropores with movable fluid saturation of 56.1% and 52.9%, respectively. In contrast, STS and STCS mainly comprise mesopores and micropores with lower movable fluid saturation of 33.5% and 27.5%, influenced by clay filling and carbonate cementation, resulting in poor connectivity. Macroscopically, better-sorted delta-front sand bodies develop connected pores within rigid quartz and feldspar particle frameworks, increasing the proportion of mesopores and macropores. Microscopically, reservoir properties, RQI, maximum invasion saturation, displacement pressure, and average pore radius significantly influence fluid movability. As centrifugal force increases, fluid output from pores slows, and the LLMPR decreases exponentially. At an optimal centrifugal force of 2.75 MPa, the LLMPR in the Linnan Depression is calculated to be 0.033 μm. Based on these insights, a fluid mobility model for lacustrine delta front-turbidite facies tight sandstones is established, identifying DFMS and DFLS as the optimal lithofacies for movable fluids. This study provides theoretical references for understanding and effectively developing deep tight sandstone reservoirs.

## 1. Introduction

With decreasing production from conventional oil reservoirs, tight oil reservoirs with immense resource potential have become an important topic in the field of oil exploration and development(Zou et al., 2015; Hu et al., 2020; Alvarado et al., 2010). Currently, there are 66 known basins containing tight oil resources, with a global technically recoverable reserve amounting to 639.3 billion tons. As the most

* Corresponding author. State Key Laboratory of Petroleum Resources and Engineering, China University of Petroleum (Beijing), Beijing,102249, China.
*E-mail address:* lindachen@cup.edu.cn (D. Chen).

https://doi.org/10.1016/j.marpetgeo.2024.107090
Received 13 March 2024; Received in revised form 21 July 2024; Accepted 3 September 2024
Available online 6 September 2024

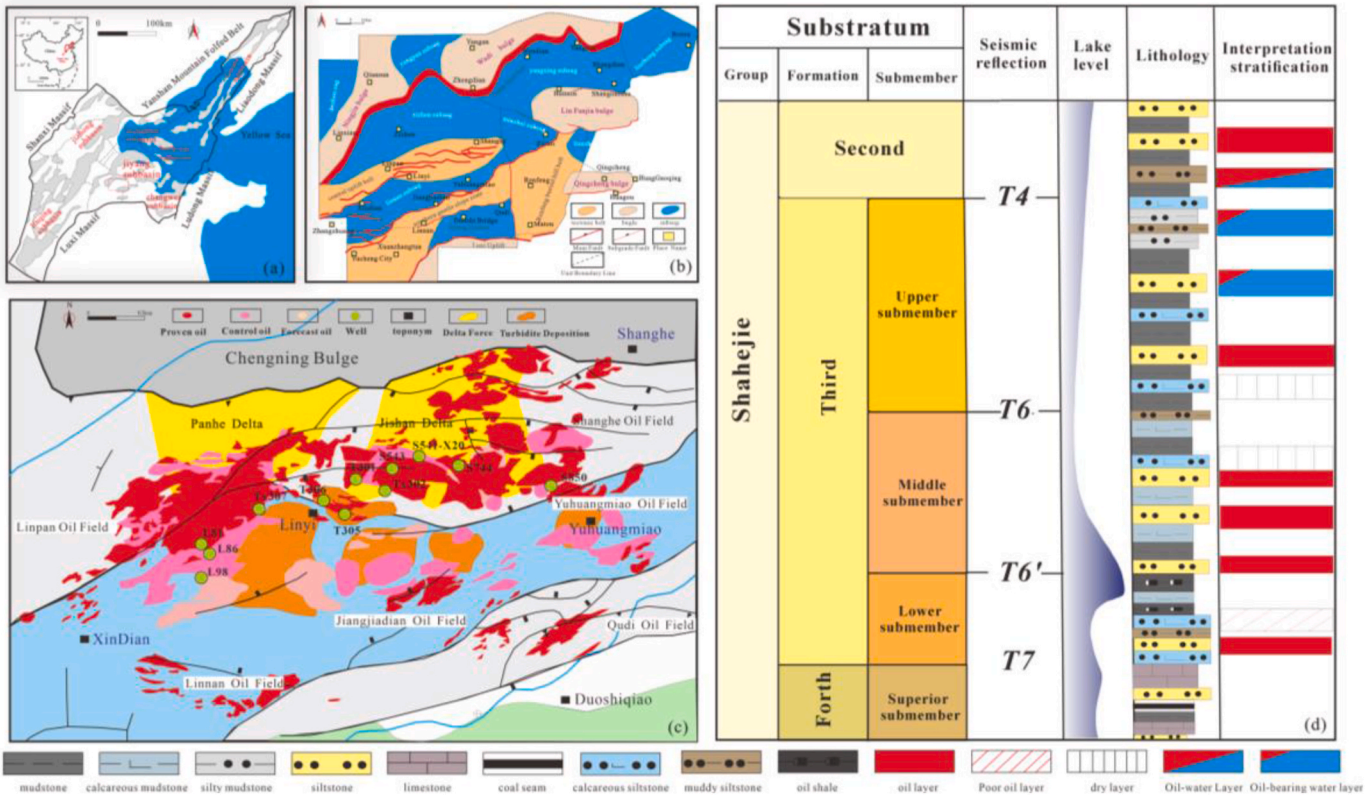


**Fig. 1.** (a)Geographic location of the Bohai Bay Basin. (b)Tectonics of the Huimin Depression region. (c)Geologic map of the Linnan Depression region. (d)Stratigraphic histogram of the T305 well.

successful region for developing tight oil resources, the United States reached a production of 378 million tons in 2022, accounting for 64% of its crude oil output(Kazemzadeh et al., 2023). In recent years, China has achieved remarkable progress in the exploration of continental tight oil, with onshore tight oil distributed across an area of 200,000 square kilometers(Wang et al., 2023a; Wu et al., 2022). Chengzao Jia used the method of resource abundance analogy to estimate the total geological resources as 106.7 to 111.5 billion tons(Jia et al., 2012). Currently, breakthroughs have been made in nine basins, including the Ordos Basin, Junggar Basin, Sichuan Basin, Songliao Basin, and Bohai Bay Basin(Yao et al., 2020; Wang et al., 2018). In 2023, the production of tight oil reached 14 million tons. In particular, the Bohai Bay Basin's Jiyang Depression has abundant tight oil resources in the Paleogene system(Ma et al., 2023; Wang et al., 2022b; Wang et al., 2019). As of 2019, the proven reserves have reached 194 million tons, and the predicted prospective resources exceed 500 million tons(Jia et al., 2023). The Linnan Depression is the main tight oil production area in the Jiyang Depression of the Bohai Bay Basin(Wang et al., 2020a, 2020b, 2021c). The primary layer is the third member of the Shahejie Formation($Es_3$). Compared to tight oil reservoirs in basins such as the Ordos Basin and the Junggar Basin, the continuous subsidence of the fault basin in the study area led to the development of a lake-delta front and the slumping of turbidite sands in the $Es_3$(Li et al., 2014). These sands are generally buried at depths of 3200–5000 m, classifying them as deep tight reservoirs(Han et al., 2023). The reservoirs are characterized by low porosity, complex diagenesis, poor pore-throat connectivity, and strong heterogeneity, resulting in significant differences in the effectiveness of the development of each well. From a geological perspective, the key factor affecting the production and recovery rate of tight oil in the Linnan Depression is the mobility of crude oil(Dong et al., 2023; Qu et al., 2022).

The parameters of mobile fluid play a vital role in assessing the characteristics of fluid presence and percolation features in the reservoir (Wei et al., 2023). Quantitative characterization of the distribution of movable fluids in microscale pores can provide evidence for addressing key geological issues restricting the productivity of tight sandstone reservoirs(Lai et al., 2018; Li et al., 2023a, 2023b). Many scholars have used nuclear magnetic resonance (NMR) technology to determine the $T_2$ cutoff value for saturated fluid rocks, which refers to the $T_2$ time threshold on the NMR $T_2$ distribution plot used to distinguish bound water from free fluids (such as free water or oil). Signals below this cutoff value typically represent fluids trapped in small pores or by capillary pressure that cannot flow, while signals above this cutoff value represent fluids that can flow freely in larger pores.(Ge et al., 2015; Guo et al., 2020). The scholars have defined movable fluid saturation (MFS) to characterize the mobility of fluids(Ge et al., 2015; Zang et al., 2022a; Meng et al., 2021; Wang et al., 2023a, 2023b). However, due to the presence of a large number of poorly connected cellular and ink-bottle-like pores in sandstone, as well as hydrophilic minerals such as potassium feldspar and illite, the strong adhesive forces in the fine throats and on the mineral surfaces result in the incomplete mobility of crude oil in pores larger than the $T_2$ cutoff value(Dai et al., 2018; Wu et al., 2023). Therefore, it is necessary to use a combination of centrifuge experiments and nuclear magnetic resonance (NMR) methods(Jiang et al., 2021). By comparing the differences in the shapes of the NMR curves of the samples before and after centrifugation, the accurate MFS can be determined, along with the lower limit of movable fluid in the pores(Zang et al., 2022a,b; Wang et al., 2023b). Concurrently, in the context of existing research, numerous scholars have acknowledged that reservoir quality, pore structure parameters, the contents of clay minerals, the evolution of secondary porosity, the occupancy of carbonate cementation, and the implications of compaction processes collectively exert substantial influence on the mobilization and retention of fluids within reservoirs(Jiang et al., 2023; Guo et al., 2022). However, within the Linnan Depression, the lacustrine environment has led to diverse sedimentary microfacies, including delta front and slumping turbidite

**Table 1**
Sandstone samples' physical properties and mineral composition.

| Type | Sample | Well | Depth/m | K/mD | φ/% | Distance to the sand-mud interface/m | Mineral composition/% | | | | | | | Clay mineral composition/% | | | |
|---|---|---|---|---|---|---|---|---|---|---|---|---|---|---|---|---|---|
| | | | | | | | Clay | Quartz | Potassium Feldspar | Plagioclase Feldspar | Calcite | Dolomite | Ferroan Dolomite | Illite-Smectite Mixed Layer | Illite | Kaolinite | Chlorite |
| I | 1 | S744 | 3161.7 | 1.48 | 11.07 | 0.7 | 9.8 | 57.4 | 5.8 | 26.2 | 0.7 | 0.0 | 0.0 | 36 | 16 | 48 | |
| | 2 | S543 | 3231.98 | 1.21 | 11.95 | 7.7 | 5.3 | 45.8 | 14.6 | 26.6 | 3.3 | 4.4 | 0.0 | 49 | 18 | 17 | 16 |
| | 3 | TX302 | 3493.42 | 1.34 | 12.68 | 5.3 | 17.8 | 48.6 | 0.9 | 27.4 | 0.9 | 4.4 | 0.0 | 44 | 17 | 29 | 10 |
| | 4 | TX302 | 3495.92 | 0.99 | 10.42 | 6.1 | 6.1 | 54.7 | 4.1 | 29.0 | 5.6 | 0.5 | 0.0 | 41 | 15 | 44 | |
| | 5 | TX302 | 3492.72 | 1.06 | 11.32 | 2.3 | 8.6 | 57.6 | 7.2 | 24.4 | 0.7 | 0.0 | 1.6 | 47 | 22 | 32 | |
| II | 6 | T301 | 3439.74 | 1.20 | 11.02 | 0.8 | 4.2 | 73.2 | 1.6 | 20.1 | 0.4 | 0.4 | 0.0 | 36 | 10 | 35 | 19 |
| | 7 | S541-X20 | 3221.8 | 0.82 | 10.06 | 1.7 | 12.7 | 58.6 | 7.1 | 19.9 | 0.8 | 0.9 | 0.0 | 60 | 13 | 27 | |
| | 8 | T301 | 3403.9 | 1.37 | 9.83 | 2.0 | 7.4 | 56.9 | 4.3 | 29.4 | 2.0 | 0.0 | 0.0 | 39 | 14 | 37 | 10 |
| | 9 | S541-X20 | 3218 | 0.87 | 10.82 | 1.8 | 5.5 | 62.1 | 6.1 | 24.5 | 0.5 | 0.0 | 1.3 | 53 | 17 | 22 | 8 |
| | 10 | S541-X20 | 3332 | 0.60 | 8.21 | 15.5 | 10.0 | 57.1 | 3.0 | 14.4 | 11.8 | 3.7 | 0.0 | 48 | 19 | 29 | 4 |
| III | 11 | TX307 | 4230.6 | 0.39 | 8.87 | 2.0 | 5.5 | 70.2 | 0.7 | 13.9 | 2.7 | 7.0 | 0.0 | 55 | 30 | | 15 |
| | 12 | TX307 | 4228 | 0.53 | 10.92 | 8.0 | 5.9 | 56.0 | 4.3 | 19.4 | 13.2 | 1.2 | 0.0 | 65 | 29 | 6 | |
| | 13 | T306 | 4005.04 | 0.33 | 8.65 | 7.4 | 15.2 | 51.5 | 0.0 | 25.9 | 5.2 | 2.2 | 0.0 | 55 | 27 | | 18 |
| | 14 | L86 | 3935.58 | 0.93 | 9.11 | 11.5 | 20.1 | 52.3 | 3.8 | 12.3 | 8.7 | 2.8 | 0.0 | 67 | 11 | 17 | 5 |
| | 15 | T305 | 4209.55 | 0.30 | 7.48 | 4.1 | 18.7 | 51.4 | 0.0 | 25.8 | 2.2 | 1.9 | 0.0 | 50 | 37 | | 13 |
| IV | 16 | T306 | 4017.33 | 0.14 | 7.77 | 26.0 | 6.7 | 42.5 | 1.1 | 23.7 | 25.6 | 0.4 | 0.0 | 78 | 14 | 4 | 4 |
| | 17 | L81 | 3899.41 | 0.10 | 7.87 | 11.8 | 9.3 | 46.2 | 2.4 | 30.2 | 11.0 | 0.8 | 0.0 | 21 | 29 | 38 | 12 |
| | 18 | TX307 | 4364.7 | 0.02 | 7.15 | 21.7 | 10.0 | 42.5 | 0.0 | 25.7 | 19.1 | 2.7 | 0.0 | 37 | 25 | | 38 |
| | 19 | T305 | 4215.8 | 0.03 | 5.18 | 15.2 | 9.9 | 53.7 | 0.0 | 21.2 | 10.3 | 0.0 | 4.9 | 81 | 31 | 12 | |
| | 20 | T306 | 4017.76 | 0.05 | 4.62 | 13.4 | 15.2 | 53.2 | 0.0 | 18.2 | 8.8 | 0.0 | 4.6 | 51 | 24 | 25 | |
| | 21 | L81 | 3851.7 | 0.19 | 3.89 | 34.7 | 8.6 | 34.8 | 2.2 | 19.7 | 28.2 | 6.5 | 0.0 | 55 | 15 | 30 | |
| | 22 | T305 | 4203.5 | 0.20 | 5.59 | 15.1 | 22.4 | 48.0 | 0.0 | 14.5 | 15.1 | 0.0 | 0.0 | 23 | 38 | | 39 |

microfacies(Li et al., 2022, 2023b). Consequently, reservoirs exhibit distinct characteristics influenced by various factors, such as the sedimentary environment, diagenetic processes, and pore development. From macroscopic sedimentary structures to microscopic mineralogy and pore structures, reservoirs of different lithofacies exhibit notable differences, resulting in distinct profiles of movable fluid distribution (Yang et al., 2020). Hence, it is imperative to conduct a systematic and comprehensive investigation into the characteristics of fluid presence and mobility within reservoirs of different lithofacies in the lacustrine depositional environment of the Linnan Depression.

To address the aforementioned issues, this study employs 22 sandstone samples from the tight reservoirs in the $Es_3$ in the Linnan Depression, as a case study. Experimental techniques, including thin section analysis, XRD, helium porosity, nitrogen permeability, SEM and HPMI, are applied to elucidate the sedimentary architecture, petrological attributes, and pore structure of these tight sandstone reservoirs. On this basis, nuclear magnetic resonance (NMR) combined with centrifuge experiments at different rotational speeds is conducted to comprehensively evaluate the fluid mobility and establish the lower limit of movable fluid in pore structures. Finally, a comprehensive assessment of the geological factors controlling fluid mobility is conducted, and a model for evaluating the fluid mobility for the deep tight sandstone reservoirs in theLinnan Depression is established, with the aim of providing theoretical support for the next step of oil development and evaluation.

## 2. Geological background

The Bohai Bay Basin is a Mesozoic–Cenozoic continental rift oil and gas basin developed on the eastern block of the North China Craton(Li et al., 2022, Fig. 1a). The Linnan Depression is located in the southwestern part of the Huimin Sag in the Jiyang Depression(Wang et al., 2020a, 2020b). Controlled jointly by the Xiakou and Linshang Fault, the Linnan Depression developed into an ENE-trending, irregularly shaped negative graben structure during the Paleogene rifting process(Wang et al., 2020a; Feng et al., 2018, Fig. 1b and c). The Linnan Depression is marked by the full development of both the Paleocene and Neoproterozoic systems, including the Kongdian, Shahejie, Dongying, Guantao, and Minghuazhen Formation, in descending order(Liu et al., 2023). The lower $Es_3$ of the Paleoproterozoic Shahejie Formation was formed during the lake flooding period of the paleolake basin. 60~260 m-thick dark mudstone were deposited, which is the main hydrocarbon source rock system(Wang et al., 2020a,b; Liu et al., 2021, Fig. 1d). During the depositional periods of the $Es_3$, the terrain was influenced by the development of the central uplift zone and the activity of the Linshang Fault(Wang et al., 2022). As a result, terrigenous clastic materials from the Chengning Uplift experienced two major phases of accumulation within the depression, leading to the formation of two centers of sand body thickness(Liu et al., 2023). These phases correspond to the Ji Shan delta-slump deposits in the Middle $Es_3$ member in the northeast and the Pan River delta-slump deposits in the Lower $Es_3$ member in the northwest, both of which are part of the Paleogene system(Zhou et al., 2013). Influenced by complex diagenetic processes at great burial depths, reservoir rock types are intricate. Under the influence of the same provenance, both reservoir sets predominantly consist of feldspathic sandstone and lithic feldspathic sandstone, with values less than 12%, classifying them as tight reservoirs. Vertically, the lower Shahejie organic-rich source rocks are interbedded within two sets of delta-slide depositional sand bodies(Wang et al., 2020a; Feng et al., 2018). The proximity of the source to the reservoir facilitates the vertical migration of crude oil, leading to the accumulation of abundant tight oil. Currently, in the Linnan Depression, six oil fields have been discovered: Lin Shanghe, Lin Pan, Yuhuangmiao, Qudi, Jiangjiadian, and Lin Nan. The proven geological oil reserves total approximately 70 million tons ($0.7 \times 10^8$ t) (Pei et al., 2017). The tight oil reservoirs are located primarily in the Shanghe region of the Shanghe Oilfield, the Tianjia and Dalujia regions of the Lin Pan Oilfield, and the Jiangjiadian region of the Jiangjiadian Oilfield (Fig. 1c). To date, a total of 135 million tons of third-level tight oil reserves have been reported, revealing significant resource potential(Feng et al., 2018).

## 3. Samples and methods

### 3.1. Samples

In this research, 22 specimens were gathered from the 9 most representative drill cores from wells in the Linnan Depression. The samples were acquired by slicing along the bedding planes, measuring 2.5 cm in diameter and 8 cm in height. The samples are primarily composed of fine siltstone and encompass a wide range of lithofacies types. To avoid structural damage to the sandstone surface caused by weathering and to enhance the accuracy of measurements of reservoir parameters, such as porosity and pore structure, all the samples were analyzed using fresh surfaces. The 8 cm drill core was longitudinally cut into three cylindrical plug samples. The middle section, with a length of 5 cm, was used for porosity, permeability, NMR, and HPMI analyses. The remaining 3 cm was divided into two short cylinders, each 1.5 cm in height (top and bottom). We used these two 1.5 cm short cylinders for the preparation of thin sections, fluorescent thin sections, cathodoluminescence, and X-ray diffraction studies. Before the experimental measurements, a washing solvent was prepared by mixing dichloromethane and methanol at a ratio of 93:7 to remove any residual oil from the rock samples (Keshavarz., 2019). During the washing process, the temperature was set at 90 °C, the pressure at 0.5 MPa, and the washing time was seven days. After washing, the samples were dried in a constant-temperature chamber (60 °C/48 h) before proceeding with the experiments. Table 1 lists the rock physics and mineral characteristics of 22 samples. The basic constituents of the rock are quartz, plagioclase, calcite, and clay. The quartz contents range from 34.80% to 73.23%, with an average of 53.38%. The acidic plagioclase contents range from 12.30% to 30.20%, averaging 22.38%, while the potassium feldspar contents average only 3.15%. Calcite, the main carbonate mineral, has contents varying from 0.4% to 28.20%, with a mean value of 8.04%. The clay contents span from 4.23% to 22.4%, averaging 10.68% (Table 1). The samples collected were classified into four types based on lithofacies classification. Type I is characterized by delta front facies massive siltstone (DFMS), Type II by delta front facies laminated siltstone (DFLS), Type III by slump turbidite facies siltstone (STS), and Type IV by slump turbidite facies calcareous siltstone (STCS).

### 3.2. Experimental methods

#### 3.2.1. X-ray diffraction analysis

X-ray Diffraction(XRD) enables the quantitative analysis of the mineral composition and content (Pawloski et al., 1985). In this study, a D8AA25 X-ray diffractometer was employed for detection. After drying the rock samples in a 60 °C oven for 48 h, the samples were ground to a particle size less than 40 μm and pressed into pellets using a back-pressure method. The computer-acquired diffraction spectra ranged from 3° to 45°. The contents of various minerals were determined using the corresponding formulas and reference intensity values for minerals.

#### 3.2.2. Thin section observation

A cast thin section was created by injecting blue resin into the evacuated pores of the rock sample to identify pore types and sizes (Wang et al., 2021a). To distinguish carbonate minerals, thin sections were stained with Alizarin Red. After the resin solidified, the samples were cut and polished using the French Brot CTS sample preparation system. The rock particle composition, pore structure, and connectivity were observed using a LinKan-350 polarizing microscope. Utilizing fluorescent thin sections is an effective method for studying rock

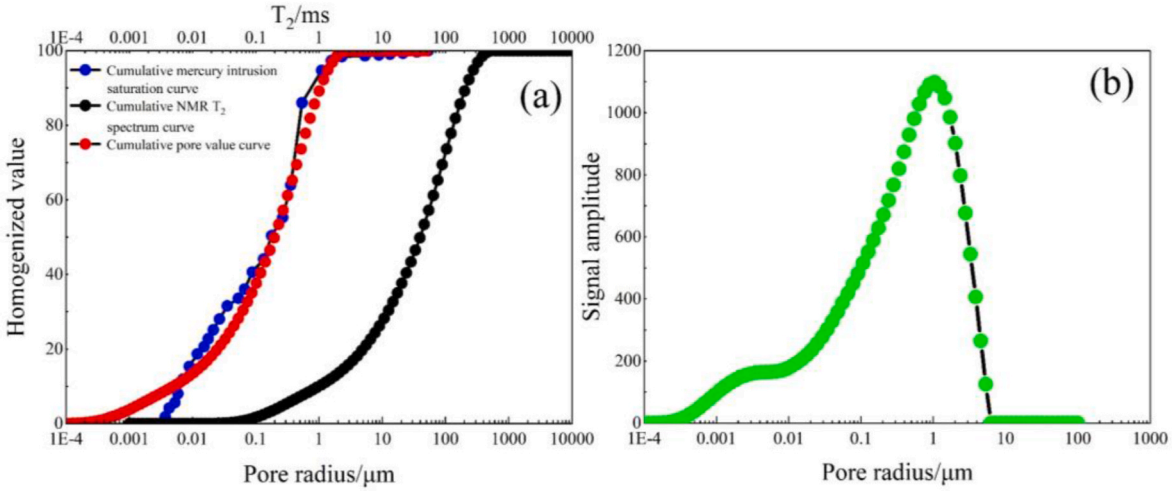


**Fig. 2.** Conversion between NMR T2 spectrum and pore radius. (a) transverse relaxation time $T_2$ cumulative curve to aperture cumulative curve conversion diagram, sample1. (b) pore and throat radius distribution diagram, sample1.

structures in reservoirs and the occurrence of fluids in oil reservoirs (Xia et al., 2021; Liu et al., 2020). The sample was first sliced into 0.3 mm thick sections and subsequently sequentially cut and polished using a cutting machine and diamond sand to create circular slices with diameters of Φ3 mm and thicknesses of 100 μm. After staining with hydroxy fluorescent dye, the rock components and the spatial distribution of oil and water were analyzed using a Leica Dmrx polarized fluorescence microscope and Cias-2007 image analyzer. Based on the identification from cast thin sections and fluorescent thin sections, we analyzed the sandstone samples using a CL8200-MK5 cathodoluminescence instrument to determine the types and extent of diagenesis, such as calcite cementation and feldspar dissolution. The experimental conditions were a temperature of 25 °C, humidity of 45%, vacuum of 0.3Pa, beam voltage of 13 kV, and beam current of 340 μA.

### 3.2.3. Porosity and permeability tests

The porosity of the thoroughly dried samples was measured using a JS 100007 helium porosity measurement instrument, with high-purity helium (99.99%) chosen as the working medium for porosity measurements. The measurement principle is based on Boyle's gas expansion law. The permeability parameters of the samples were obtained using an A-1013 gas permeameter.To reflect the characteristics of porosity and permeability in the reservoir, this paper introduces the Reservoir Quality Index (RQI) to evaluate reservoir quality. Amaefule proposed this parameter to characterize reservoir quality and fluid flow capacity (Amaefule et al., 1993). When the permeability is measured in millidarcies (mD), the Reservoir Quality Index is defined by equation (1).

$$RQI = 0.0316\sqrt{\frac{K}{\varphi}} \tag{1}$$

In equation (1), RQI represents the Reservoir Quality Index; k (mD) denotes permeability in millidarcies; φ (%) denotes porosity.

### 3.2.4. Scanning electron microscopy observation

Scanning Electron Microscopy(SEM) can be used for the qualitative observation of mineral composition, pore types, and sizes (Chukwuma et al., 2018). Prior to observation, the sample was sliced into thin sections, and the observation surface was argon-ion polished and gold-coated to enhance sample conductivity. Finally, observations were performed using a ZEISS Merlin microscope with a maximum resolution of 1 nm. The pore morphology and mineral elemental composition were observed using secondary electron detectors and EDS.

### 3.2.5. High Pressure Mercury Injection analysis

High Pressure Mercury Injection (HPMI) testing is a method in which a mercury porosimeter is used to inject mercury into a porous solid under different pressures to determine the pore characteristics of the sample (Jiao et al., 2020; Gao et al., 2021). The injection pressure and pore radius in the mercury intrusion experiment satisfied the Washburn equation(Matthews et al., 1995). In this study, Corelab CMS300 and Auto Pore IV 9510 instruments were used. The mercury intrusion tests included both pressurized intrusion and pressurized withdrawal tests, with a maximum experimental pressure of 200 MPa. The Washburn equation was used to convert the mercury intrusion pressure curve into a throat radius (Zhao et al., 2021).

$$D = 2r = -\frac{4\sigma\ cos\ \theta}{p} \tag{2}$$

In equation (2), $D$(cm) represents the pore diameter; r(cm) denotes the pore radius; $\theta$ is the wetting angle; $\sigma$ represents the surface tension of mercury in $10^{-3}$ N/m; $p$(MPa) represents the injection pressure in Pascals.

### 3.2.6. Nuclear magnetic resonance and centrifugation

Nuclear Magnetic Resonance(NMR) is a physical process in which atomic nuclei with non-zero magnetic moments split their spin energy levels under the influence of an external magnetic field, and absorb radiofrequency radiation of a certain frequency to enter a higher energy state (Becker et al., 1993; Griesinger et al., 2012). After the radiofrequency pulse ceases, under the influence of the main magnetic field, the transverse macroscopic magnetization vector gradually decreases to zero, corresponding to the transverse relaxation time (Noack et al., 1971; Korb et al., 2018). For the same fluid properties and rock sample, the relaxation time is determined by the pore size (Washburn et al., 2014). The NMR $T_2$ spectra of tight sandstone saturated with a single-phase fluid (anhydrous kerosene) can better reflect the internal pore structure of the rock. In a homogeneous magnetic field, the transverse relaxation time $T_2$ is given by:

$$\frac{1}{T_2} = \rho\left(\frac{S}{V}\right) + \frac{1}{T_{2B}} \tag{3}$$

In equation (3), $T_2$ (ms) is the transverse relaxation time in milliseconds; $T_{2B}$(ms) is the bulk relaxation time in milliseconds; $\rho$(μm/ms) is the transverse surface relaxation rate in micrometers per millisecond; $S$ (μm$^2$) is the surface area of a single pore in square micrometers; $V$(μm$^3$) is the volume of a single pore in cubic micrometers.

Since the value of $T_{2B}$ is significantly greater than $T_2$, the value of 1/

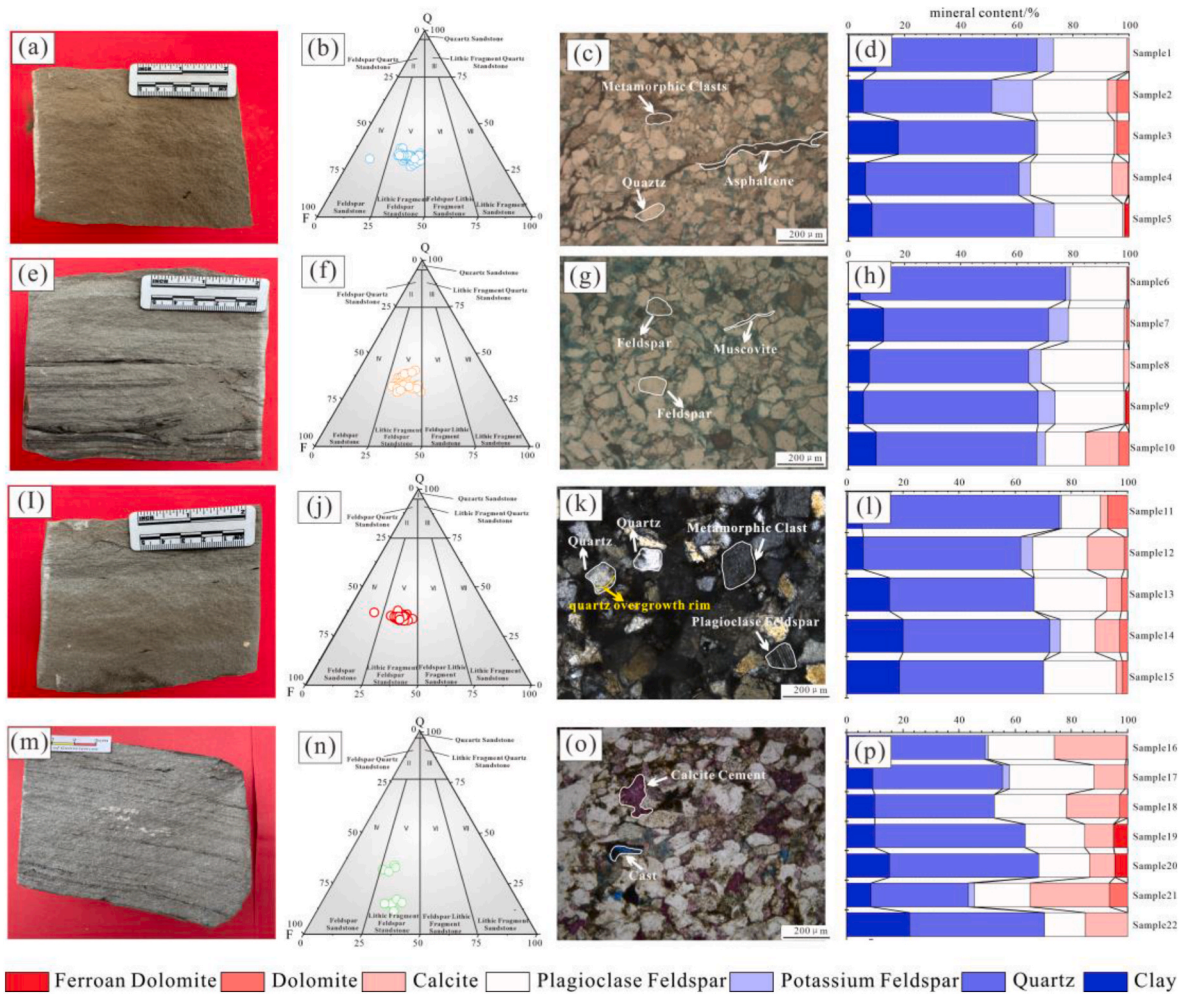


**Fig. 3.** Petrographic Characteristics of Tight Sandstone Based on Core Description, Thin Section Observation, and XRD Diffraction:(ăd)delta front facies massive siltstone (DFMS),Well TX302,3493.42m; (e ~ h)delta front facies laminated siltstone(DFLS), Well S541-X20, 3221.8m; (i ~ l)slump turbidite facies siltstone(STS), Well T305, 4209.55m; (m ~ p)slump turbidite facies argillaceous siltstone(STCS), Well T306, 4017.33m).

$T_{2B}$ can be neglected, and equation (3) can be simplified to:

$$\frac{1}{T_2} = \rho\left(\frac{S}{V}\right) \tag{4}$$

From equation (4), it can be seen that $T_2$ is related to the specific surface area S/V of a single pore. Let the value of $S/V$ equal to the value of $F_S/r$, then we have:

$$T_2 = \frac{r}{\rho_2 F_S} \tag{5}$$

In equation (5), r(μm) is the pore radius in micrometers; $F_S$ is the shape factor of a pore, which is related to the geometric shape of the pore.

Let the value of $C$ be equal to the value of $\rho_2 F_S$, then we have equation (6):

$$r = CT_2 \tag{6}$$

From equation (6), it can be seen that the transverse relaxation time $T_2$ is theoretically linearly proportional to the pore radius. Once the value of $C$ is determined, the NMR $T_2$ spectra can be converted into the pore throat radius distribution curve (Zheng et al., 2018). The conversion coefficient $C$ is influenced by the transverse relaxation rate of the rock and the pore shape factor, and cannot be directly measured through experiments. Therefore, domestic and foreign scholars usually calibrate the NMR $T_2$ spectra with high-pressure mercury intrusion curves to determine the conversion coefficient C (Slijkerman et al., 2001; Liu et al., 2019). For example, using Sample 1 (S744, 3161.7 m), after standardizing the signal intensity of the NMR $T_2$ spectra, the cumulative curve of NMR is obtained by accumulating from left (small pores) to right (large pores) (Fig. 2a). Similarly, by accumulating the pore throat radius data from high-pressure mercury intrusion experiments from left to right, the cumulative curve of the pore throat radius is obtained (Fig. 2a). Then, the comparable interval of the two curves is defined using the pore throat radius range obtained from high-pressure mercury intrusion. Applying the principle of maximum similarity, the two curves are overlapped as closely as possible using the least squares method, thus obtaining the pore throat radius conversion coefficient $C$ of the NMR $T_2$ spectra. Based on the obtained conversion coefficient $C$, the NMR $T_2$ spectra can be converted into a pore throat radius distribution curve (Fig. 2b).

The nuclear magnetic resonance experiment was conducted at the State Key Laboratory of Petroleum Resource and Prospecting, China University of Petroleum (Beijing), using MicroMR12 equipment with a main frequency of 12.0 MHz. To ensure the stability of the magnetic field, the laboratory temperature was maintained at 25 °C ± 0.5 °C, and the magnetic field temperature was controlled at 32 °C ± 0.1 °C. The waiting time was set to 3000 ms, the echo spacing was 0.1 ms, the echoes number was 6000, and the accumulation was carried out 64 times.

This study employs centrifugal force to characterize displacement pressure using a high-speed centrifuge to generate centrifugal force and

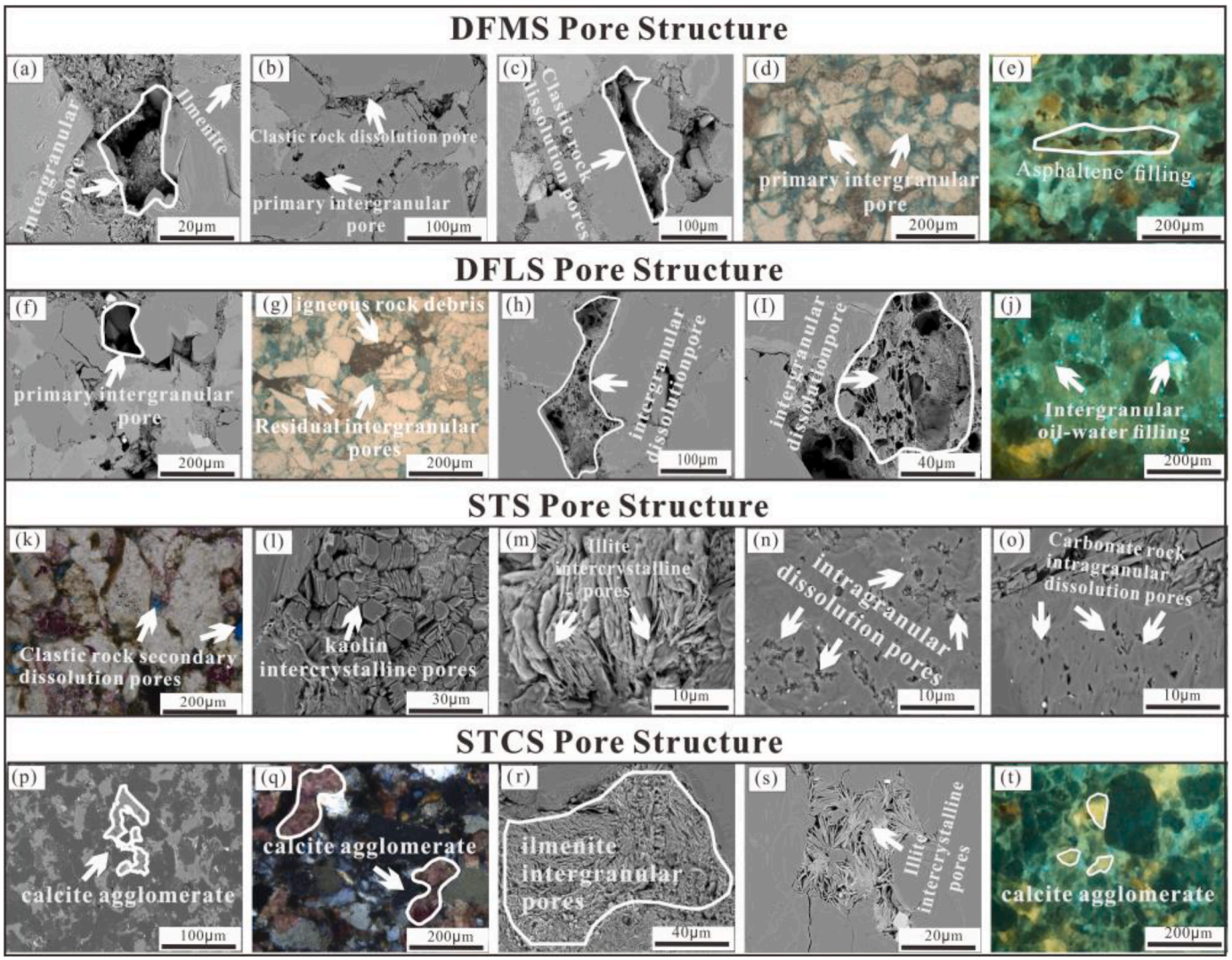


**Fig. 4.** Thin section, SEM observation of pore structure. (a)Residual intergranular pores, TX302,3493.42m,Scanning electron microscope (SEM). (b)Primary intergranular pores,TX302,3493.42m,Scanning electron microscope (SEM). (C)Residual intergranular pores, TX302,3495.92m,Scanning electron microscope (SEM). (d)Primary intergranular pores and Secondary dissolution pores, S744, 3161.7m,Cast thin section. (e)Asphaltene-filled pores, S543,3231.98m,Fluorescent thin section. (f)Residual intergranular pores, T301, 3403.9m,Scanning electron microscope (SEM). (g)Residual intergranular pores, T301, 3403.9m,Cast thin section. (h) Rock fragment dissolution pores, X541-X20, 3221.8m,Scanning electron microscope (SEM). (i)Rock fragment dissolution pores, X541-X20, 3221.8m,Scanning electron microscope (SEM). (j) Abundant oil and water in dissolution porosity, X541-X20, 3221.8m,Fluorescent thin section. (k)Intergranular dissolution pores and carbonate dissolution porosity, T305, 4209.5m,Cast thin section. (l)Booklet kaolinite, TX307, 4228m,Scanning electron microscope (SEM). (m)illite intercrystalline pores, T306, 4004.5m,Scanning electron microscope (SEM). (n)Intragranular dissolution pores, TX307, 4230.6m,Scanning electron microscope (SEM).(o)Intragranular dissolution pores, TX307, 4230.6m,Scanning electron microscope (SEM). (p)Carbonate mineral cementation, L81, 3851.7m,Scanning electron microscope (SEM). (q)Carbonate mineral cementation, L81, 3851.7m,Cast thin section. (r) Intercrystalline pores in illite, T306, 4017.76m,Scanning electron microscope (SEM). (s)Intercrystalline pores in illite, L81, 3851.7m,Scanning electron microscope (SEM). (t)Carbonate cements showing faint yellow fluorescence, L81, 3851.7m, Fluorescent thin section.

expel fluids from the rock. At various rotational speeds, the centrifugal pressure difference of two-phase fluids equals the capillary pressure.

$$P_{ci} = 1.097 \times 10^{-9} \Delta\rho L \left(R_e - \frac{L}{2}\right) \eta^2 \tag{7}$$

The formula for calculating the capillary pressure is given by Equation (8):

$$P_c = \frac{2\sigma \cos\theta}{r} \tag{8}$$

In the equation, $P_{ci}$ represents the centrifugal capillary pressure (MPa); $\Delta_\rho$ (g/ml) represents the density difference between two-phase fluids; $L$ (cm) represents the sample length; $R_e$ (cm) represents the outer rotating radius of the rock sample; $\eta$ (rpm) represents the rotation speed; $P_c$ (MPa) represents the capillary force; $\sigma$ (mN/m) represents the interfacial tension between gas and water, typically 72(Kashefi et al., 1976); θ (°) represents the wetting angle, with a wetting angle of 0 for gas–water centrifugation; and r (μm) represents the pore radius(Hachem et al., 2022).

The specific steps were as follows: ① The oil washing solvent was prepared by mixing dichloromethane and methanol at a ratio of 93:7. The rock sample was washed with the prepared solvent and then placed in a constant temperature box for drying (60 °C/48 h). The dimensions were measured, the rock samples were weighed, and the sample volume was calculated. ② The rock core was evacuated for 4 h, saturated with water-free kerosene under a pressure of 30 MPa for 48 h, weighed, and subjected to oil saturation nuclear magnetic resonance (NMR) $T_2$ spectrum measurements. ③ With a centrifuge at speeds of 2000, 4000, 6000,

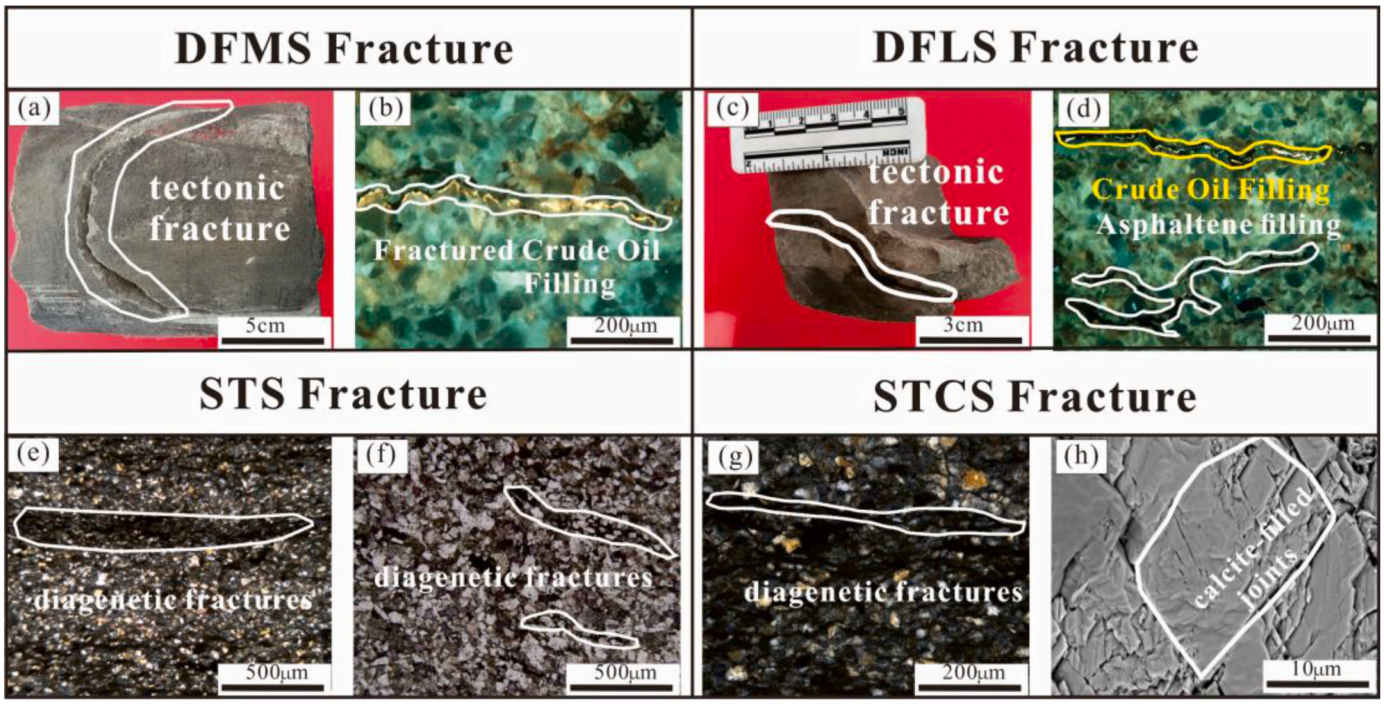


**Fig. 5.** Observations of micro-fracture characteristics in core samples, thin sections, and scanning electron microscopy. (a) Tectonic fracture, TX302,3493.42m. (b) Micro-fractures rich in oil, S543, 3231.98m. (c) High-angle structural fracture with hydrocarbon indications, T301, 3403.9m. (d) Micro-fractures filled with crude oil and bitumen, T301, 3403.9m. (e) Diagenetic fractures, T306,4005.4m. (f) Diagenetic fractures, L86, 3935.58m. (g) Bedding plane fractures filled with bitumen, T305, 4215.8m. (h) Feldspar vein fractures, T305, 4215.8m.

8000, 10000 and 11000 rpm, the rock sample was centrifuged for 2 h at each speed. After centrifugation, the sample was weighed, and the $T_2$ spectra were measured at different speeds. ④ Based on the centrifugation and experimental results, the movable fluid saturation was calculated.

According to the principles of NMR, the area under the $T_2$ spectrum reflects the volume of fluids within the rock core. Different from the idealized conditions assumed by the $T_2$ cutoff method (assuming that bound fluids exist only in small pores and that movable fluids exist only in large pores), we employed an area-based approach to calculate the difference between the saturation state and the $T_2$ spectrum area after centrifugation (Equation (9))(Zheng et al., 2019). This difference, when compared to the area of the saturation state $T_2$ spectrum (excluding the area of the dry state $T_2$ spectrum), was used as the movable fluid saturation(MFS).

$$MFS = \frac{\int_{T_{2\,min}}^{T_{2\,max}} S(T_{2S})dT_2 - \int_{T_{2\,min}}^{T_{2\,max}} S(T_{2C})dT_2}{\int_{T_{2\,min}}^{T_{2\,max}} S(T_{2S})dT_2 - \int_{T_{2\,min}}^{T_{2\,max}} S(T_{2d})dT_2} \quad (9)$$

In the equation, $S(T_{2s})$ represents the expression for the $T_2$ spectrum distribution under saturated conditions, $S(T_{2c})$ represents the expression for the $T_2$ spectrum distribution under centrifuged conditions, and $S(T_{2d})$ represents the expression for the $T_2$ spectrum distribution under dry conditions.

## 4. Results

### 4.1. Mineral petrology and sedimentary characterization

Through detailed observations and descriptions of core samples, it has been definitively determined that the study area is characterized by four distinct lithofacies: Type I is characterized by delta front facies massive siltstone (DFMS), Type II by delta front facies laminated siltstone (DFLS), Type III by slump turbidite facies siltstone (STS), and Type IV by slump turbidite facies calcareous siltstone (STCS) (Fig. 3a–e, I, and m). Thin section observations reveal that the sandstones are predominantly lithic feldspathic sandstone and feldspathic sandstone (Fig. 3b–f, j, and n). Metamorphic rock fragments constitute the primary lithic component, accounting for 25% of the total lithic composition. The mineral grains are mostly subrounded to subangular, with grain sizes ranging from 0.06 mm to 0.5 mm. The grains exhibit point-line contacts and are accompanied by clay mineral fillings and carbonate mineral cementation.(Fig. 3c–g, k, and o). The sorting and structural maturity of the sandstone transition from medium to poor as it progresses from the facies indicating a deltaic front of a lacustrine environment to slump-turbidite deposition, reflecting the rapid accumulation of sediment in a slump-gravity flow system(Fig. 3a–e, i, and m). X-ray diffraction (XRD) analysis reveals that the four main mineral components in the sand bodies are primarily quartz, feldspar, calcite, and clay minerals (Fig. 3d–h, l, and p). Quartz and acidic plagioclase feldspar have the highest average proportions, accounting for 53.38% and 22.38%, respectively. Potassium feldspar is not well developed. Carbonate minerals exist as cement within primary residual intergranular pores and secondary dissolution pores, with calcite being the major component, averaging between 2.24% and 16.87%. Dolomite content is relatively low and is considered a minor carbonate mineral. Additionally, sulfate mineral gypsum, iron oxide mineral hematite, and sulfide mineral pyrite have also been found. In the slump-turbidite facies, active ion exchange from thin sandstone-thick mudstone combinations results in higher carbonate mineral contents (average of 12.50%) than from sand bodies at the deltaic front. The supply of terrestrial clastic sediments from the Chengning Uplift results in a relatively low clay mineral content in the reservoir (averaging 10.68%), with the highest clay content occurring in the facies representing the low-energy environments of the slump-turbidite facies (average of 12.28%)(Zhang et al., 2019). The clay component consists of kaolinite, chlorite, illite, and I/M mixed layers (illite/montmorillonite mixed layers), with the I/M mixed layers accounting for only 20–30% of the clay fraction. This suggests that the reservoir underwent diagenetic evolution during the middle stage of lithification, during which illite minerals gradually formed.

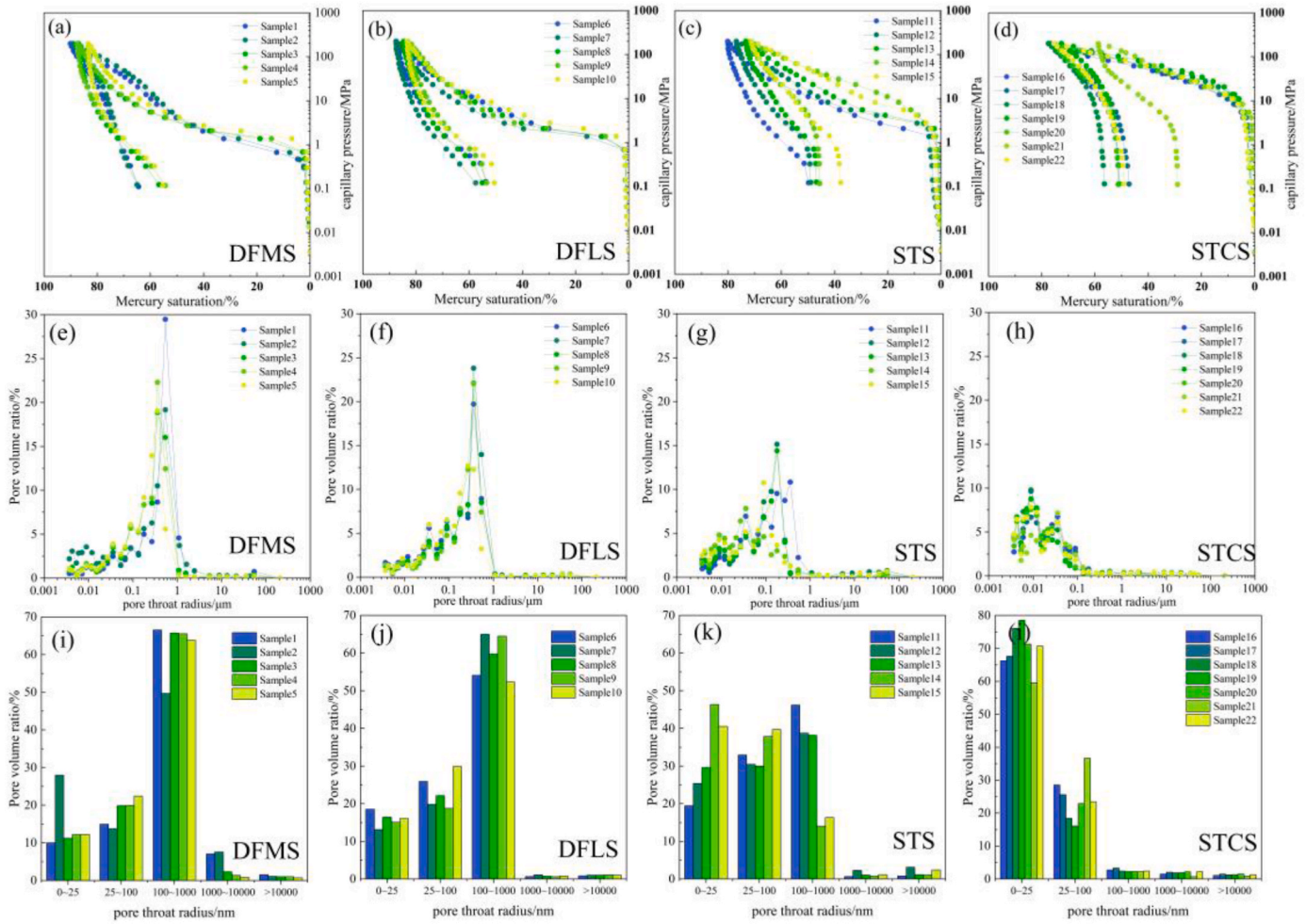


**Fig. 6.** Capillary pressure curves and full pore size distribution plots of the tight reservoir in the fourth type of delta turbidite facies in the Linnan depression.(a) DFMS capillary pressure curve.(b) DFLS capillary pressure curve.(c) STS capillary pressure curve.(d) STCS capillary pressure curve.(e) DFMS pore size distribution curve.(f) DFLS pore size distribution curve.(g) STS pore size distribution curve.(h) STCS pore size distribution curve.(i) DFMS pore size distribution histogram.(j) DLMS pore size distribution histogram.(k) STS pore size distribution histogram.(l) STCS pore size distribution histogram.

### *4.2. Pore system characterization*

Through thin section and scanning electron microscopy (SEM) observations, we identified a variety of pore types in the sandstone layers, primarily including residual primary intergranular pores, secondary dissolution pores (intergranular and intragranular), intercrystalline pores of clay minerals, and limited occurrences of microfractures. Influenced by deep burial diagenesis, the four lithofacies exhibit distinct pore types and pore structure characteristics. The DFMS lithofacies shows the most developed pore systems, dominated by residual primary intergranular pores (Fig. 4a) and secondary dissolution pores, contributing significantly to porosity. The primary intergranular pores appear in triangular, quadrilateral, and irregular polygonal shapes, with relatively large pore sizes. Secondary dissolution pores include small-scale dissolution pores and large-scale moldic pores (Fig. 4b, c, and d), with bitumen filling observed within these pores (Fig. 4e). The DFLS lithofacies develops a small amount of primary intergranular pores (Fig. 4f and g) and a large number of secondary intergranular dissolution pores (Fig. 4h and i). Feldspar and lithic grains exhibit pronounced dissolution due to the action of acidic formation waters, with strong dissolution along cleavage planes; oil and water traces are observed within these dissolution pores (Fig. 4j).For the STS lithofacies, primary intergranular pores are drastically reduced under strong compaction, with secondary dissolution pores (Fig. 4k) and intercrystalline pores of clay minerals (Fig. 4l and m) providing the main pore space. These secondary dissolution pores are predominantly intragranular, mainly developed in plagioclase and to a lesser extent in potassium feldspar, characterized by honeycomb-like dissolution structures formed through hydrocarbon infiltration and erosion (Fig. 4n and o). The intercrystalline pores of clay minerals, primarily in kaolinite and illite, are minute, with pore throats being narrow and most pore diameters less than 1 μm. For the STCS lithofacies, impacted by intense carbonate cementation and clay matrix filling, primary residual intergranular pores and some dissolution pores are completely occluded (Fig. 4p and q), with intercrystalline pores of clay minerals being the main reservoir space. Clay films are frequently present along the margins of brittle mineral grains, with secondary illite and kaolinite extensively filling these pores (Fig. 4r and s), resulting in extremely poor oil-bearing characteristics (Fig. 4t).

Through indoor core observation and microscopic identification, we have identified structural fractures, diagenetic fractures, and structurally-diagenetic compound fractures (joint fractures, grain boundary fractures, and intragranular fractures) in the sandstone layers. Influenced by the intense activity of the Lingshang Fault of the Paleogene Shahejie Formation (Wang et al., 2023b), tectonically induced structural fault fractures and joint fractures have developed, commonly observed in the DFMS (Fig. 5a), where fractures frequently exhibit excellent hydrocarbon shows (Fig. 5b). In DFLS, mid-to-high angle structural fractures were also observed (Fig. 5c), and along the bedding planes, bedding fractures are well developed, with good hydrocarbon shows frequently observed along these fractures (Fig. 5d). Influenced by

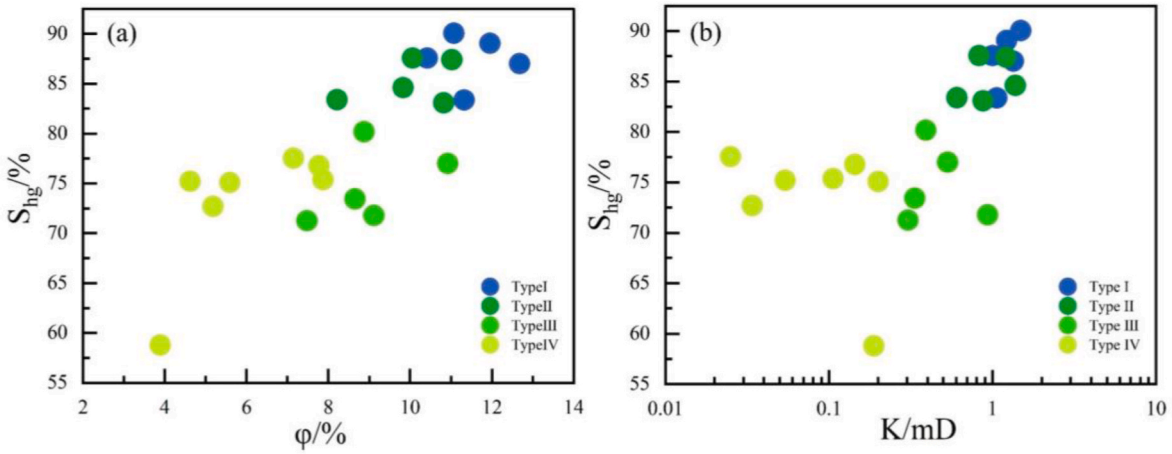


**Fig. 7.** Correlation between reservoir properties of dense sandstone and maximum mercury intrusion saturation in the linnan Depression.(a) Correlation diagram between porosity and maximum mercury saturation.(b). Correlation diagram between permeability and maximum mercury saturation.

**Table 2**
Mercury compression and NMR parameters of tight reservoir in Linnan depression.

| Type | Number | Mercury injection curve parameters | | | | | | NMR pore size distribution ratio | | | |
|---|---|---|---|---|---|---|---|---|---|---|---|
| | | $R_p$ /μm | $R_a$ /μm | $R_{50}$ /μm | $S_{hg}$ /% | $S_r$ /% | $P_{cd}$ /MPa | I-micropores | II-micropores | mesopores | macropores |
| I (DFMS) | 1 | 0.445 | 0.182 | 2.007 | 90.06 | 64.43 | 0.32 | 0.45 | 0.18 | 2.01 | 90.06 |
| | 2 | 0.307 | 0.164 | 1.13 | 89.07 | 65.02 | 0.455 | 0.31 | 0.16 | 1.13 | 89.07 |
| | 3 | 0.225 | 0.219 | 0.724 | 87.02 | 54.42 | 0.676 | 0.23 | 0.22 | 0.72 | 87.02 |
| | 4 | 0.232 | 0.214 | 0.587 | 87.57 | 55.36 | 0.676 | 0.23 | 0.21 | 0.59 | 87.57 |
| | 5 | 0.226 | 0.168 | 0.674 | 83.37 | 56.79 | 0.676 | 0.23 | 0.17 | 0.67 | 83.37 |
| II (DFLS) | 6 | 0.21 | 0.12 | 0.364 | 87.40 | 55.02 | 0.678 | 0.21 | 0.12 | 0.36 | 87.40 |
| | 7 | 0.235 | 0.221 | 0.903 | 87.57 | 57.58 | 0.675 | 0.24 | 0.22 | 0.90 | 87.57 |
| | 8 | 0.226 | 0.15 | 0.57 | 84.61 | 53.67 | 0.672 | 0.23 | 0.15 | 0.57 | 84.61 |
| | 9 | 0.234 | 0.186 | 1.449 | 83.08 | 53.38 | 0.672 | 0.23 | 0.19 | 1.45 | 83.08 |
| | 10 | 0.194 | 0.097 | 0.584 | 83.40 | 50.51 | 0.672 | 0.19 | 0.10 | 0.58 | 83.40 |
| III (STS) | 11 | 0.181 | 0.067 | 0.928 | 80.18 | 49.81 | 0.676 | 0.18 | 0.07 | 0.93 | 80.18 |
| | 12 | 0.106 | 0.049 | 0.168 | 77.00 | 49.03 | 2.048 | 0.11 | 0.05 | 0.17 | 77.00 |
| | 13 | 0.103 | 0.03 | 0.339 | 73.43 | 46.85 | 2.057 | 0.10 | 0.03 | 0.34 | 73.43 |
| | 14 | 0.059 | 0.015 | 0.042 | 71.79 | 45.59 | 2.053 | 0.06 | 0.02 | 0.04 | 71.79 |
| | 15 | 0.082 | 0.015 | 0.05 | 71.26 | 37.71 | 1.363 | 0.08 | 0.02 | 0.05 | 71.26 |
| IV (STCS) | 16 | 0.025 | 0.01 | 0.041 | 76.77 | 51.08 | 5.494 | 0.03 | 0.01 | 0.04 | 76.77 |
| | 17 | 0.023 | 0.009 | 0.051 | 75.37 | 47.23 | 5.505 | 0.02 | 0.01 | 0.05 | 75.37 |
| | 18 | 0.018 | 0.009 | 0.112 | 77.54 | 56.48 | 8.26 | 0.02 | 0.01 | 0.11 | 77.54 |
| | 19 | 0.017 | 0.007 | 0.055 | 72.71 | 50.89 | 8.259 | 0.02 | 0.01 | 0.06 | 72.71 |
| | 20 | 0.02 | 0.009 | 0.041 | 75.21 | 51.29 | 8.259 | 0.02 | 0.01 | 0.04 | 75.21 |
| | 21 | 0.028 | 0.005 | 0.02 | 58.79 | 28.97 | 5.504 | 0.03 | 0.01 | 0.02 | 58.79 |
| | 22 | 0.037 | 0.019 | 0.047 | 75.09 | 46.16 | 5.497 | 0.04 | 0.02 | 0.05 | 75.09 |

Note: Note: $R_p$, $R_{50}$, $R_a$, $S_{hg}$, $S_r$, $P_{cd}$ respectively represent the maximum pore radius, average pore radius, median pore radius, maximum mercury intrusion saturation, final residual mercury saturation, and displacement pressure.

deep burial diagenesis, local volume expansion due to rock diagenesis typically results in the development of diagenetic fractures along clay-rich laminae, which are prevalent in the high-clay-content STS (Fig. 5e and f) and STCS (Fig. 5g). Furthermore, SEM observations reveal the widespread presence of feldspar and calcite joint fractures in STCS (Fig. 5h).

### *4.3. Pore size distribution characteristics*

#### *4.3.1. HPMI results*

High-pressure mercury injection (HPMI) tests record the change in mercury saturation with pressure during mercury injection (Zhang et al., 2019). The nonwetting phase mercury is injected sequentially from larger to smaller pores. The mercury injection process reflects the characteristics of all the pore throats. The pore structure parameters are obtained through HPMI. Based on the differences in the morphology of the mercury injection and withdrawal curves, HPMI parameters, and pore size distribution, the four lithofacies of sandstones are classified into four types (Fig. 6).

The Type I to Type IV sandstones exhibit a decreasing trend in maximum mercury saturation ($S_{hg}$) from 87.4% to 73.1%, and the desaturation behavior follows the same trend (Fig. 6a, b, c, and d). Simultaneously, the capillary pressure curve gradually shifts to the right from an overall leftward skew (Fig. 6a, b, c, and d). The platform cross-section ranges from the lowest in Type I to the highest in Type IV, indicating a decreasing trend in reservoir pore throat selectivity. The average capillary pressures at saturation for the Type I and Type IV sandstones are 0.5 MPa, 0.67 MPa, 1.639 MPa, and 6.683 MPa, respectively, suggesting a decrease in the size of the largest connected pores. The average pore radius of the reservoir decreases from 0.29 μm to 0.024 μm. This comprehensive analysis indicates a transition from lacustrine deltaic sandstones to turbidite sandstones, with decreasing rock sorting, physical properties, and pore structure. The reservoir transitions from being dominated by micrometer to submicrometer pores, gradually shifting toward nanopores (Fig. 6e, f, g, h, I, j, k and k). Fig. 7 shows that, from the Type IV sandstone to the Type I sandstone,

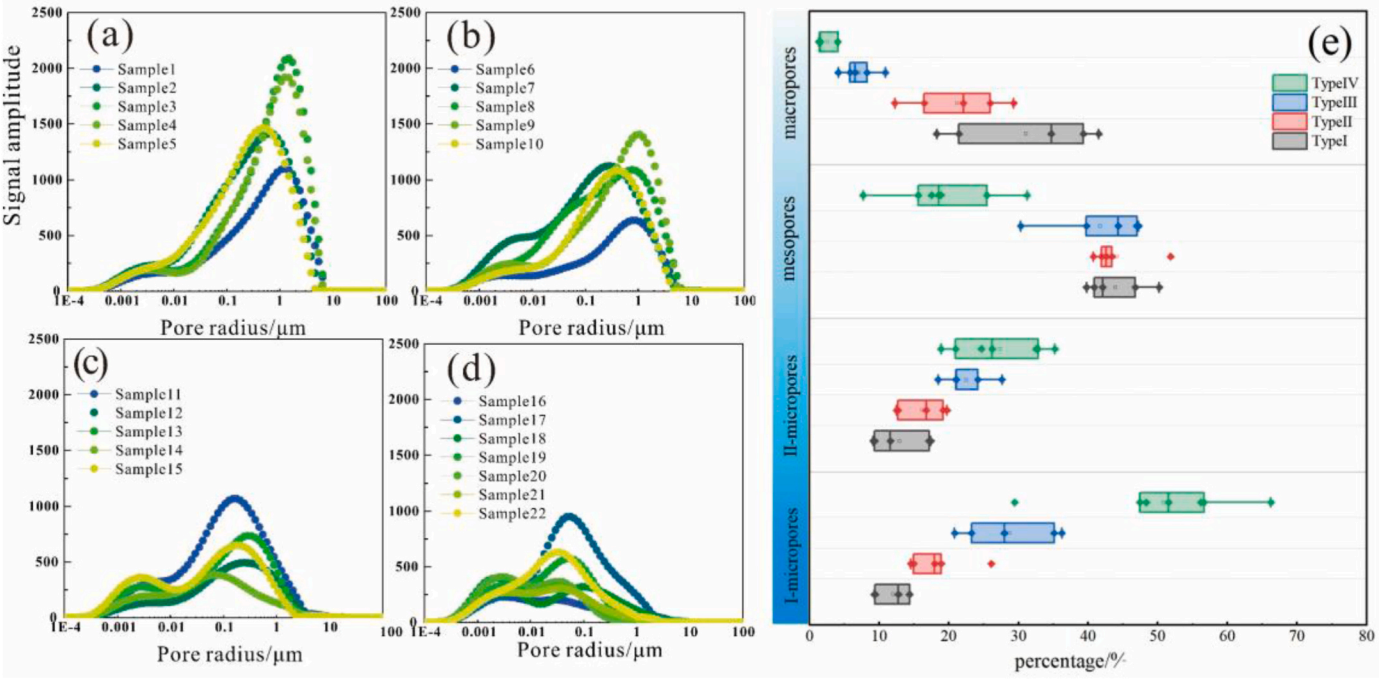


**Fig. 8.** (a~d) NMR $T_2$ spectrum of saturated anhydrous kerosene sample. (e)Pore distribution based on NMR $T_2$ spectral transformations.

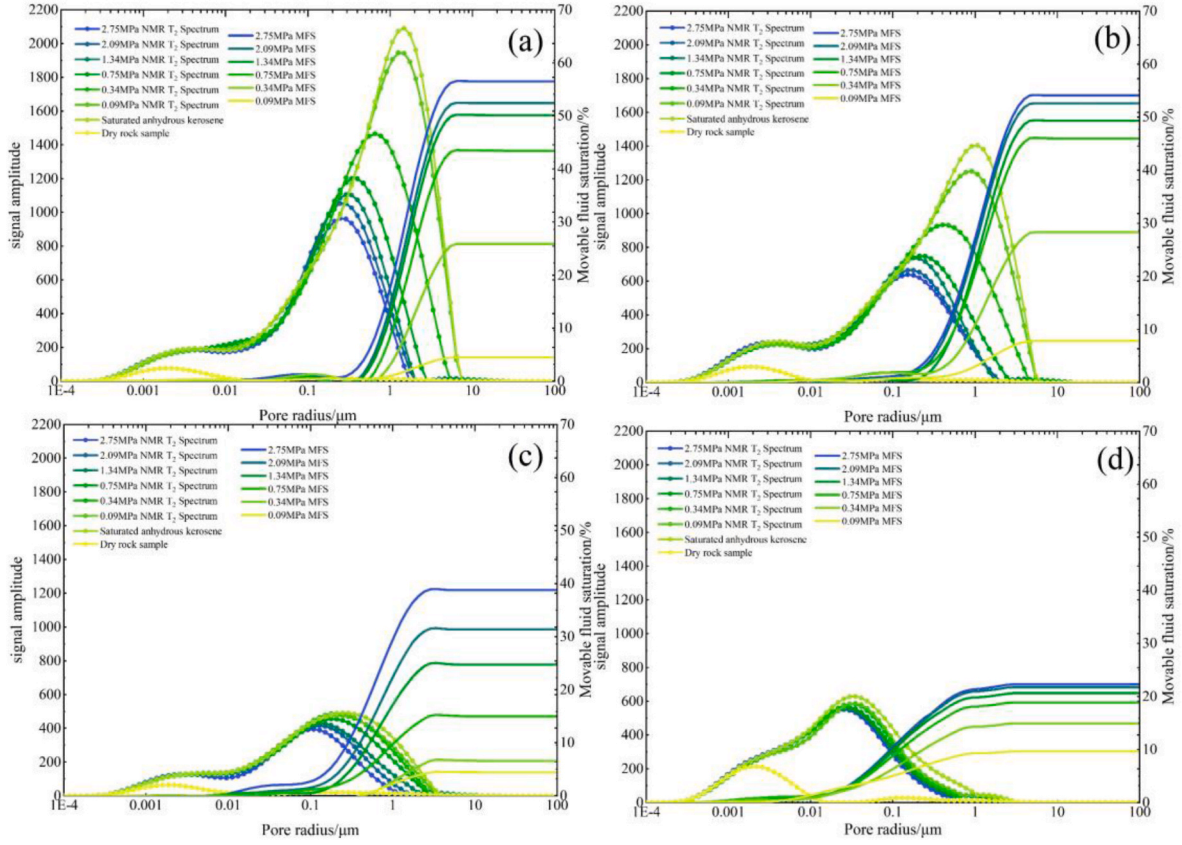


**Fig. 9.** NMR $T_2$ spectra of oil-saturated-centrifuged state. (a) Type I, sample2. (b) Type II, sample7. (c) Type III, sample12. (d) Type IV, sample22.

the reservoir porosity and permeability gradually increase, and $S_{hg}$ gradually increases (Fig. 7), indicating an improvement in the reservoir pore structure and facilitating the flow and displacement of nonwetting phase fluids. SEM observations reveal that Type I and Type II deltaic blocky and laminated sandstones primarily exhibit developed dissolution pores and residual intergranular pores (Fig. 4a and b). Additionally, structural fractures and diagenetic microfractures are present (Fig. 5a, b, c, and d), giving them relatively high storage and permeability

**Table 3**
Parameters of movable fluid distribution in four types of dense sandstones.

| Type | Sample | Centrifugal NMR parameters | | | | | | Movable fluid in different pores | | | | | |
|---|---|---|---|---|---|---|---|---|---|---|---|---|---|
| | | | | | | | | Micropores | | Mesopores | | Macropores | |
| | | 0.09 MPa | 0.34 MPa | 0.75 MPa | 1.34 MPa | 2.09 MPa | 2.75 MPa | $MFS_{mi}$ /% | $PM_1$ /% | $MFS_{me}$ /% | $PM_2$ /% | $MFS_{ma}$ /% | $PM_3$ /% |
| I (DFMS) | 1 | 13.7 | 33.2 | 35.9 | 49.0 | 59.5 | 63.8 | 2.5 | 4.0 | 26.2 | 41.1 | 35.0 | 54.9 |
| | 2 | 8.2 | 25.9 | 39.9 | 46.7 | 55.3 | 60.1 | 2.6 | 4.3 | 35.6 | 59.3 | 21.9 | 36.4 |
| | 3 | 4.5 | 25.9 | 43.5 | 50.1 | 52.4 | 56.5 | 1.3 | 2.3 | 13.8 | 24.5 | 41.4 | 73.3 |
| | 4 | 8.9 | 22.4 | 32.8 | 39.7 | 45.8 | 50.3 | 1.2 | 2.4 | 11.6 | 23.0 | 37.5 | 74.6 |
| | 5 | 10.5 | 22.0 | 29.8 | 36.9 | 44.4 | 49.7 | 0.6 | 1.1 | 31.4 | 63.1 | 17.8 | 35.8 |
| II (DFLS) | 6 | 10.3 | 21.4 | 29.7 | 39.9 | 49.3 | 54.1 | 1.9 | 3.5 | 27.6 | 51.0 | 24.6 | 45.5 |
| | 7 | 11.4 | 26.4 | 43.1 | 50.1 | 53.6 | 58.4 | 16.2 | 27.7 | 30.1 | 51.5 | 12.1 | 20.7 |
| | 8 | 10.4 | 29.9 | 40.1 | 48.3 | 49.1 | 53.4 | 5.1 | 9.5 | 26.6 | 49.8 | 21.7 | 40.8 |
| | 9 | 7.9 | 28.3 | 46.0 | 49.4 | 52.6 | 54.1 | 1.1 | 2.1 | 23.7 | 43.8 | 29.3 | 54.1 |
| | 10 | 9.3 | 20.0 | 29.9 | 34.0 | 39.0 | 44.6 | 0.5 | 1.2 | 27.7 | 62.0 | 16.4 | 36.8 |
| III (STS) | 11 | 11.8 | 14.5 | 25.0 | 32.3 | 36.7 | 39.0 | 5.0 | 12.7 | 28.0 | 71.7 | 6.1 | 15.5 |
| | 12 | 4.4 | 6.6 | 15.0 | 24.7 | 31.4 | 38.8 | 2.6 | 6.6 | 25.4 | 65.4 | 10.9 | 28.0 |
| | 13 | 4.4 | 9.5 | 15.6 | 19.3 | 27.2 | 32.8 | 2.2 | 6.8 | 17.3 | 52.8 | 13.2 | 40.4 |
| | 14 | 6.9 | 12.9 | 12.2 | 19.3 | 25.5 | 33.6 | 5.1 | 15.1 | 20.7 | 61.5 | 7.9 | 23.4 |
| | 15 | 9.7 | 13.5 | 14.9 | 15.6 | 19.8 | 23.6 | 1.4 | 5.9 | 18.9 | 80.1 | 3.3 | 14.0 |
| IV (STCS) | 16 | 8.2 | 11.0 | 17.8 | 23.4 | 31.9 | 34.5 | 14.9 | 43.2 | 16.2 | 47.0 | 3.4 | 9.8 |
| | 17 | 4.8 | 14.2 | 23.7 | 29.4 | 32.9 | 35.4 | 9.3 | 26.3 | 23.1 | 65.1 | 3.0 | 8.6 |
| | 18 | 11.7 | 17.6 | 21.9 | 25.9 | 28.3 | 32.3 | 5.4 | 16.7 | 23.3 | 72.2 | 3.6 | 11.0 |
| | 19 | 5.7 | 13.6 | 20.2 | 22.7 | 25.4 | 27.2 | 10.2 | 37.5 | 16.4 | 60.1 | 0.6 | 2.4 |
| | 20 | 5.1 | 12.7 | 16.1 | 18.2 | 19.5 | 21.0 | 12.5 | 59.6 | 7.5 | 35.7 | 1.0 | 4.6 |
| | 21 | 10.0 | 16.3 | 19.5 | 18.3 | 18.7 | 20.1 | 8.3 | 41.4 | 11.0 | 54.6 | 0.8 | 4.0 |
| | 22 | 9.6 | 14.9 | 18.9 | 20.6 | 21.8 | 22.3 | 8.9 | 40.0 | 12.4 | 55.7 | 1.0 | 4.3 |

Note: $PM_1$, $PM_2$, and $PM_3$ are the proportion of movable fluid in Micropores, Mesopores, Macropores. $MFS_{mi}$, $MFS_{me}$, and $MFS_{ma}$ are the saturation of movable fluid in Micropores, Mesopores, Macropores.

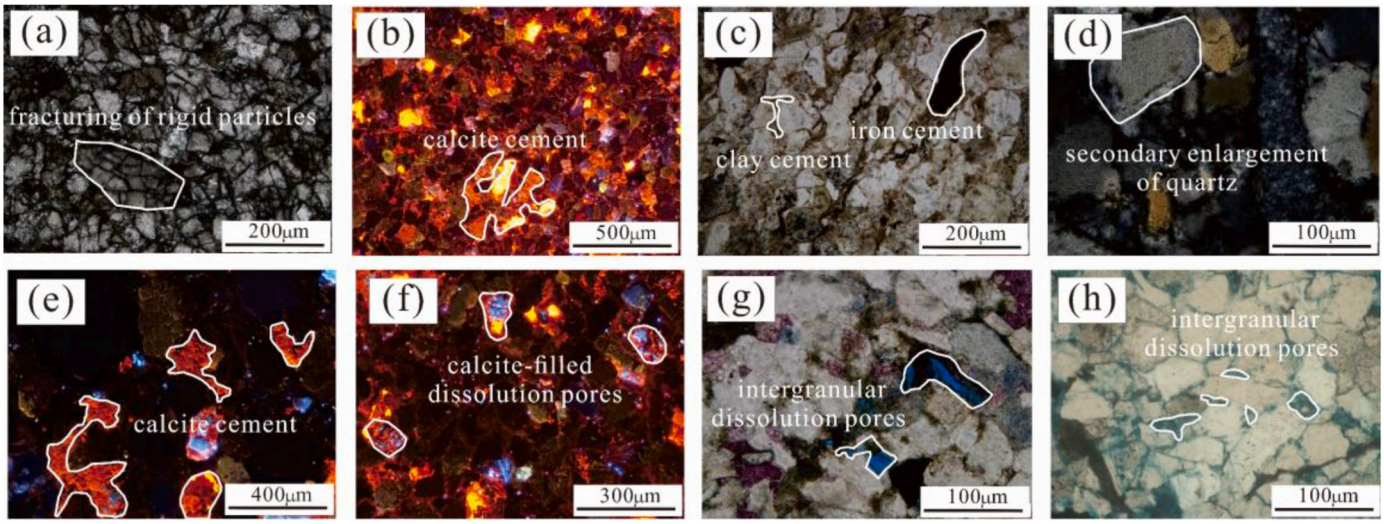


**Fig. 10.** Cast thin section and cathodoluminescence images display the types of diagenesis.(a) Rigid particle fracture, cast thin section, single polarization, sample11. (b) Calcite cementation, cathodoluminescence, cross-polarization, sample22.(c) Mudstone cementation and iron cementation, cast thin section, single polarization, sample13.(d) Secondary enlargement of quartz, cast thin section, cross-polarization, sample8.(e) Calcite filling primary intergranular pores, cathodoluminescence, cross-polarization,sample12.(f) Calcite cement filling feldspar and lithic fragments dissolution pores, cathodoluminescence, cross-polarization, sample12.(g) Feldspar dissolution pores, cast thin section, single polarization, sample16.(h) Intergranular dissolution pores, cast thin section, single polarization, sample7.

capacities (average porosities of 11.57% and 9.99%, and average permeabilities of 1.21 mD and 0.979 mD, respectively) (Table 1). In contrast, the Type III and Type IV turbidite sandstones are affected by carbonate minerals and mud fillings (Fig. 4m, n, o, p, q, and r). The presence of intergranular dissolution pores and residual intergranular pores diminishes, whereas the occurrence of intercrystalline pores and intragranular dissolution pores sees an increase.The pore throats become finer, resulting in reduced reservoir connectivity and poorer storage and permeability capacities (average porosities of 9.01% and 6.01%, and average permeabilities of 0.499 mD and 0.107 mD, respectively) (Table 1).

#### 4.3.2. NMR results

NMR measurements were conducted on saturated anhydrous kerosene samples, converting the transverse relaxation time into the pore size to obtain the $T_2$ spectrum of the pore distribution (Rudszuck et al., 2019). The shape, amplitude, and range of the $T_2$ spectrum characterize the distribution of pore sizes and the connectivity of the pores(Liu et al., 2018).When a rock sample is saturated with a homogeneous fluid, the pore size influences the NMR relaxation times, with larger pores typically corresponding to longer relaxation times. Unlike the pore structure classification scheme for shale (pores >2 nm as micropores, pores between 2 nm and 50 nm as mesopores, and pores >50 nm as macropores),

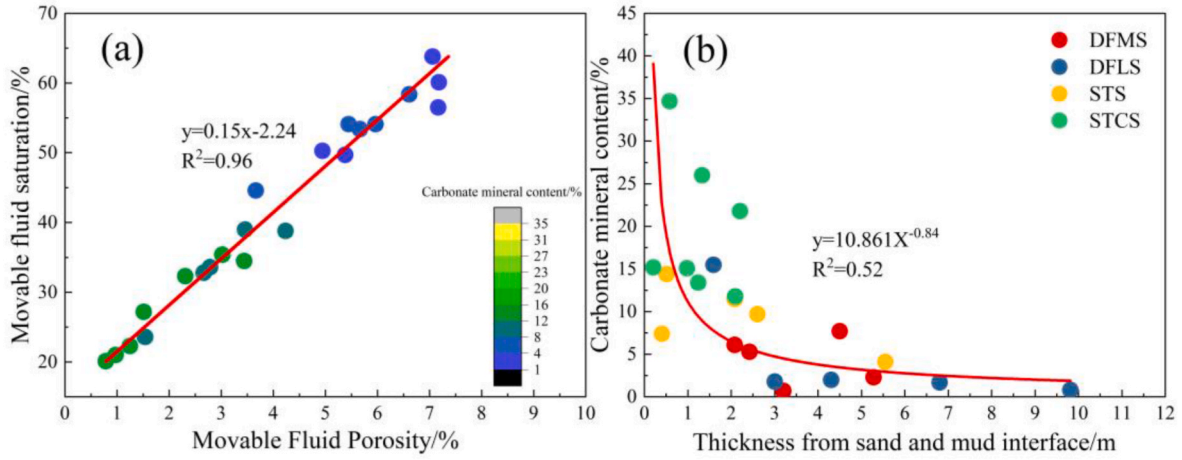


**Fig. 11.** Effect of carbonate minerals on fluid mobility and the alleged role of carbonate mineral content according to the distance from the sand-silt interface. (a) Plot of carbonate minerals versus mobilizable fluid saturation and mobilizable fluid porosity. (b) Plot of distance from sandstone to mud interface versus carbonate mineral content.

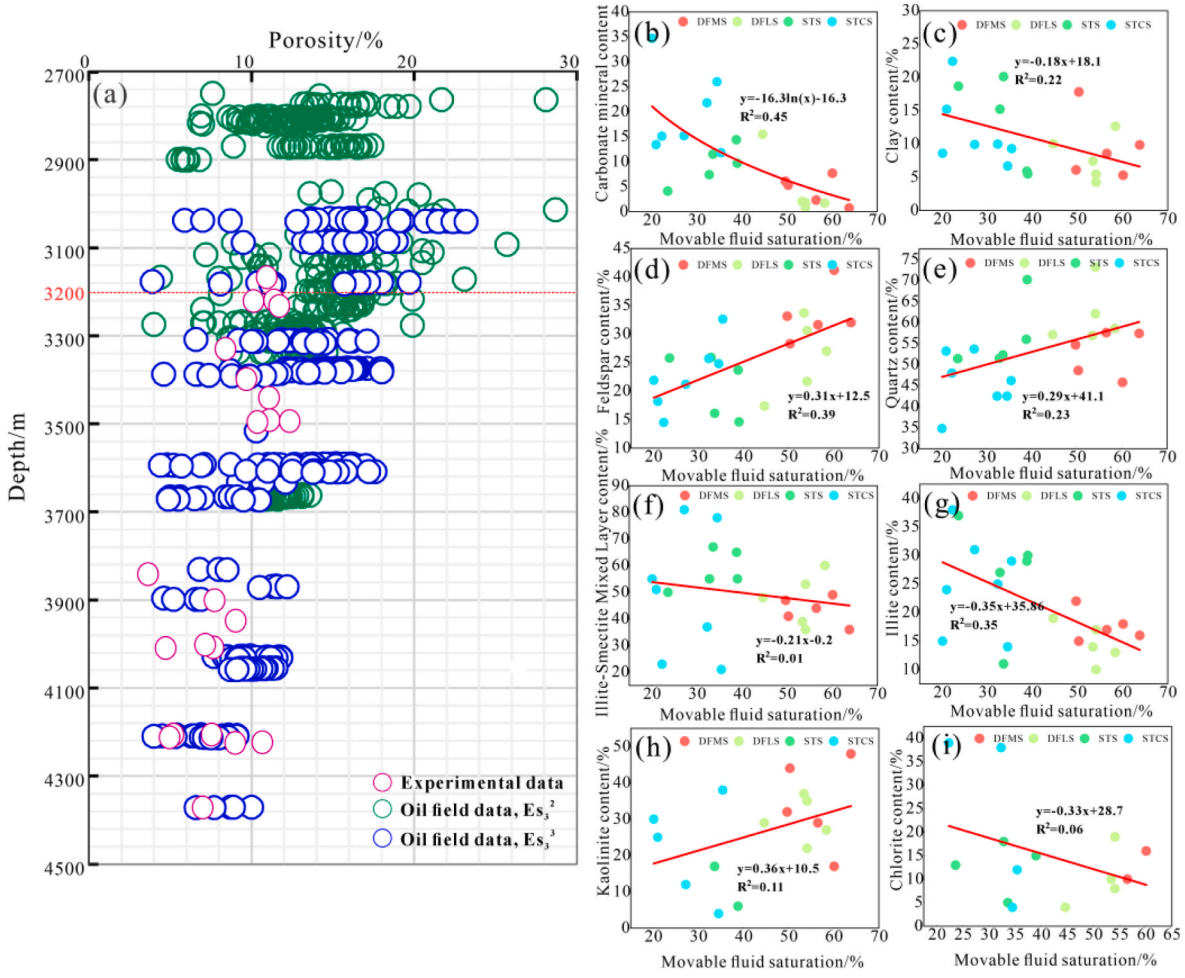


**Fig. 12.** Porosity evolution during burial and the effect of diagenetic minerals on movable fluid saturation. (a) Porosity evolution with burial depth. (b ~ e) Correlation plots of carbonate minerals, clay minerals, feldspar, and quartz with movable fluid saturation. (f ~ g) Correlation plots of illite-smectite mixed layer, illite, kaolinite, and chlorite with movable fluid saturation.

using a broader pore size range to classify pores in tight sandstones can better describe the pore characteristics and fluid flow behavior(Gao et al., 2016; Zhao et al., 2016). The pore classification for sandstones in the Linnan Sag is as follows: I-micropores (<25 nm), II-micropores (25–200 nm), mesopores (100–1000 nm), and macropores (>1000 nm) (Table 2). In the Type I DFMS, the $T_2$ spectrum shows a distinct single right peak (0.1–10 μm) (Fig. 8a), while in the Type II, III, and IV sandstones, the amplitude of the right peak decreases, and the main peak

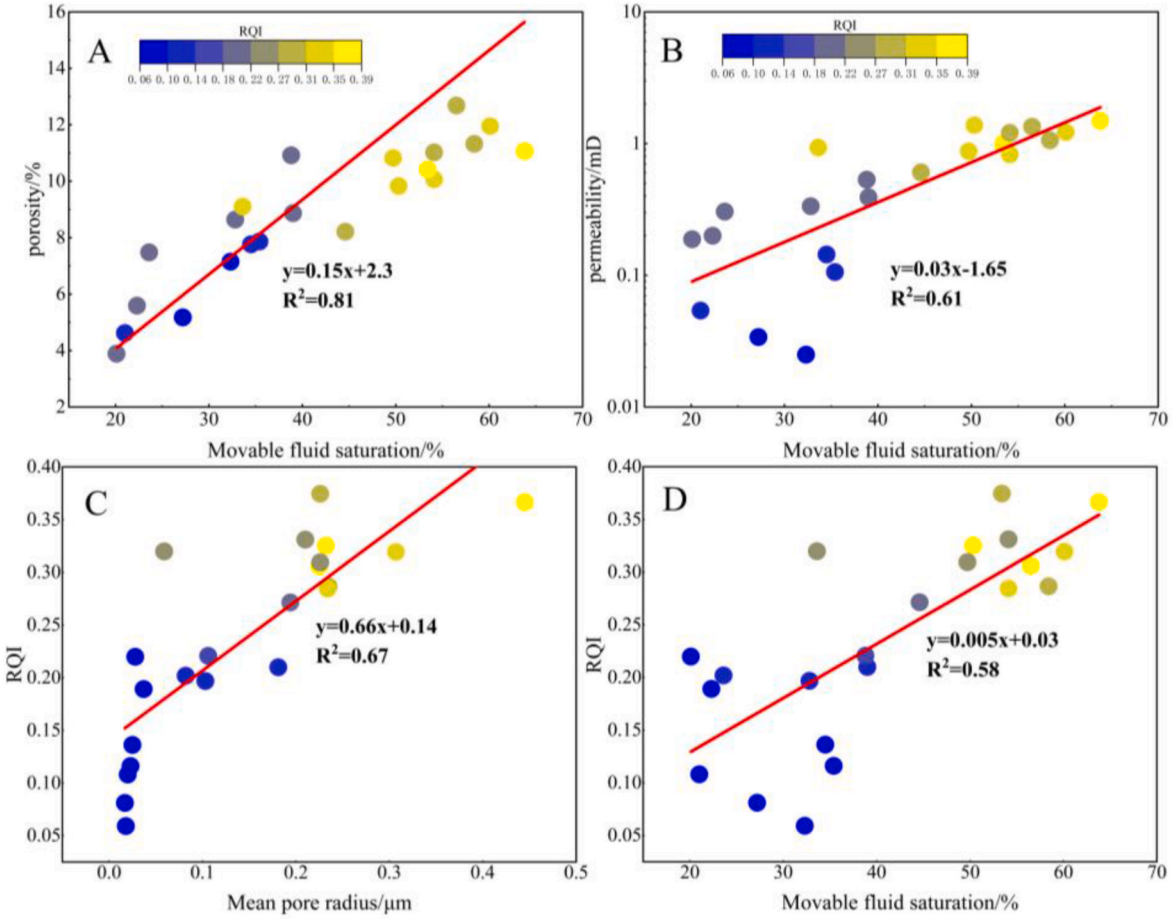


**Fig. 13.** Influence of reservoir porosity and permeability on movable fluid saturation. (a) Crossplot of porosity and movable fluid saturation.(b) Crossplot of permeability and movable fluid saturation.(c) Crossplot of RQI and average pore throat radius. (d) Crossplot of RQI and movable fluid saturation.

gradually shifts to the left (Fig. 8b, c, and d). Some samples of Types III and IV exhibit a bimodal structure, with an increased proportion of micropores (Fig. 8e). Types I and II sandstones feature full-size pores, mainly mesopores and mesopores, with mesopores (microfractures, feldspar-rock debris dissolution pores, and a certain proportion of primary intergranular pores) accounting for 26%. However, Type III (STS) sandstones are dominated by micropores, with a certain proportion of mesopores (42%). Type IV reservoirs have limited development of micropores and a few mesopores (16.9%). Under strong compaction, strong carbonate cementation, and clay filling, the proportion of macropores is less than 2% of the total pores. The lack of large pores and the development of small pores in Type III and IV reservoirs are consistent with the HPMI results.

### 4.4. *Movable fluid saturation characterization*

The movable fluids in rock pores are free fluids that flow by overcoming capillary forces and viscous resistance under certain external forces, while bound fluids generally exist in micropores and dead pores, making them difficult to flow under external forces (Bear., 2013). To quantitatively characterize the proportion of movable fluids and clarify their relationship with the pore structure, saturated anhydrous kerosene samples were centrifuged at different rotational speeds. The capillary pressure difference between two-phase fluids at different speeds equals the capillary pressure, which is calculated using Equation (5). At rotational speeds of 2000, 4000, 6000, 8000, 10000, and 11000 rpm, the corresponding centrifugal forces measure 0.09, 0.34, 0.75, 1.34, 2.09, and 2.75 MPa, respectively.

Fig. 9 and Table 3 present the NMR $T_2$ spectra and MFS (movable fluid saturation) data, respectively, of four types of typical sandstone samples under different centrifugal forces. In the low centrifugal force state (<0.09 MPa), which represents the initial stage of fluid differentiation (Fig. 9a, b, c and d), the proportion of bound fluids is high (86.3% ~91.5%). The four types of sandstones have similar MFS (mean fluid saturation) values (average MFS values ranging from 90.2% to 92.6%). The NMR $T_2$ spectra exhibit a higher peak on the right and a changing envelope area, while the left peak remains low and stable. This stage indicates that fluids in macropores (intergranular dissolution pores and microfractures) are easily initiated and expelled under low-pressure conditions. In the medium centrifugal force state (0.34–0.75 MPa), the right peaks of the $T_2$ spectra for the Type I and Type II delta front sandstones noticeably decrease (the envelope area significantly decreases), and the envelope peak begins to shift to the left (Fig. 9a and b). For the Type III and Type IV turbidite sandstones, there is also a slight decrease in the right peak (Fig. 9c and d). This stage suggests that fluids in the mesopores of sandstone start overcoming capillary forces under centrifugal forces, and the difference in the proportion of mesopores among the four types of sandstones is the main reason for the variation in the decrease in the right peak of the $T_2$ spectrum. Under high centrifugal force conditions (1.34–2.75 MPa), there's a noticeable deceleration in the leftward movement of the $T_2$ spectrum's rightmost peak (Fig. 9a, b, c, and d). At this stage, the $T_2$ spectrum aperture range is limited to less than <1 μm, indicating that after the expulsion of fluids in critical macropores and mesopores, the remaining fluids are confined to micropores, making it difficult for them to be expelled.

At the maximum centrifugal force (2.75 MPa), the MFS of all the samples span from 20.14% to 63.77%, averaging out at 41.15%. The MFS of DFMS is the highest, averaging 56.1%. DFLS follows closely, with

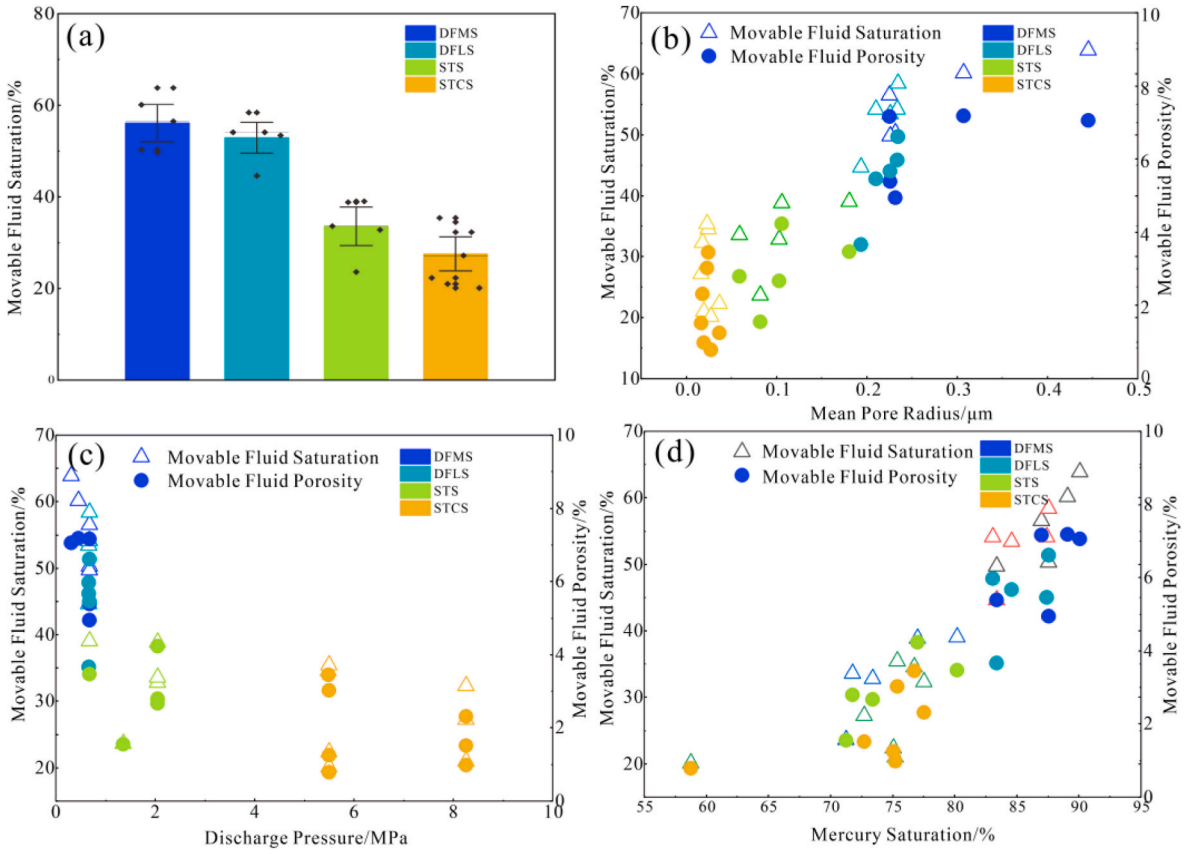


**Fig. 14.** Pore characterization parameters affecting movable fluid saturation, movable fluid porosity. (a) Distribution of movable fluid saturation in different sandstone lithologies. (b ~ d) Mean pore radius, maximum pore radius, maximum mercury feed saturation and movable fluid saturation, movable fluid porosity correlation plots.

an average of 52.9%. STS and STCS exhibit lower movable fluid saturations, with averages of 33.5% and 27.5%, respectively. The differences in the amplitudes of the micropore, mesopore, and macropore ranges were calculated separately to determine the variations in fluid occurrence states at multiple scales (Table 3).

DFMS and DFLS mobile fluids are primarily present in mesopores and macropores. For $PM_3$, the respective proportions are 55.0% and 39.6%, while for $PM_2$, the proportions are 42.2% and 51.6%, respectively. The mobile fluids in STS are mostly present in mesopores, with $PM_2$ accounting for 66.11%, while the proportion of $PM_3$ decreases to 24.47%. In STCS, mobile fluids are present in both mesopores and micropores, with $PM_2$ and $PM_1$ accounting for 55.8% and 37.8%, respectively. The primary cause of this distribution is the absence of macropores due to carbonate cementation, muddy filling causing intergranular dissolution pores, and residual intergranular pores, leading to fluid confinement in clay intercrystalline pores and intragrain pores.

## 5. Discussion

### *5.1. Macroscopic and microscopic geological elements jointly control fluid mobility*

#### *5.1.1. Macroscopic control of fluid mobility by physical sources, depositional environments and diagenesis*

The movement of fluids in tight sandstone is influenced by macrogeological factors, such as provenance, the depositional environment, and diagenetic processes (Zang et al., 2022a). The provenance and depositional environment control the composition, grain size, and pore types of sandstones, thereby affecting the saturation of movable fluids (Bjørlykke et al., 2014). In the Linan Depression, continuous subsidence in the Paleogene $Es_3$ period in the southern basin and a sustained supply of terrestrial clastics in the northern Chengning Uplift resulted in similar reservoir lithologies composed mainly of lithic arkose and arkose (Wang et al., 2020a, Fig. 3a–e, i, and m). The transition from delta front (DFMS and DFLS) to semideep lake turbidite deposition (STS and STCS) led to a decrease in the MFS of sandstones from 54.5% to 30.1% (Table 3). Simultaneously, both depositional and diagenetic processes controlled reservoir pore types, sizes, and shapes. DFMS and DFLS formed in a delta front environment, but DFLS formed in a relatively low-energy water environment with finer grain sizes than DFMS. These strata contain easily fillable fine-grained muddy sediments within bedding structures (Fig. 3f). Additionally, compared with DFMS, DFLS has experienced greater mechanical compaction and dissolution, resulting in poorer pore throat connectivity and pore structure and leading to slightly lower fluid mobility (MFS = 52.9%).

With increasing burial depth and maturation of mineral components, the impact of diagenetic processes on fluid mobility becomes more pronounced (Wintsch et al., 1994). the fracturing of rigid particles (like quartz) and the deformation of plastic particles (such as mica) (Li et al., 2023a, Fig. 10a). During compaction, pseudomicritization damages primary pores, leading to decreased pore connectivity. Through statistical analysis of collected data from oil fields and experimental sample data, it is observed that the average porosity reduction in the $Es_3$ reservoir of the Linan Depression typically ranges between 0.65% and 1.3% per 100 m (Fig. 12a). Sandstone reservoirs deeper than 3200 m predominantly exhibit porosities between 5% and 13%, characterizing them primarily as deep tight reservoirs. Thin section observations reveal cementing components, such as carbonate minerals, sulfate minerals, silica minerals, clay minerals, and iron-bearing minerals in sandstones (Fig. 10b, c, and d). Carbonate cementation and authigenic clay mineral

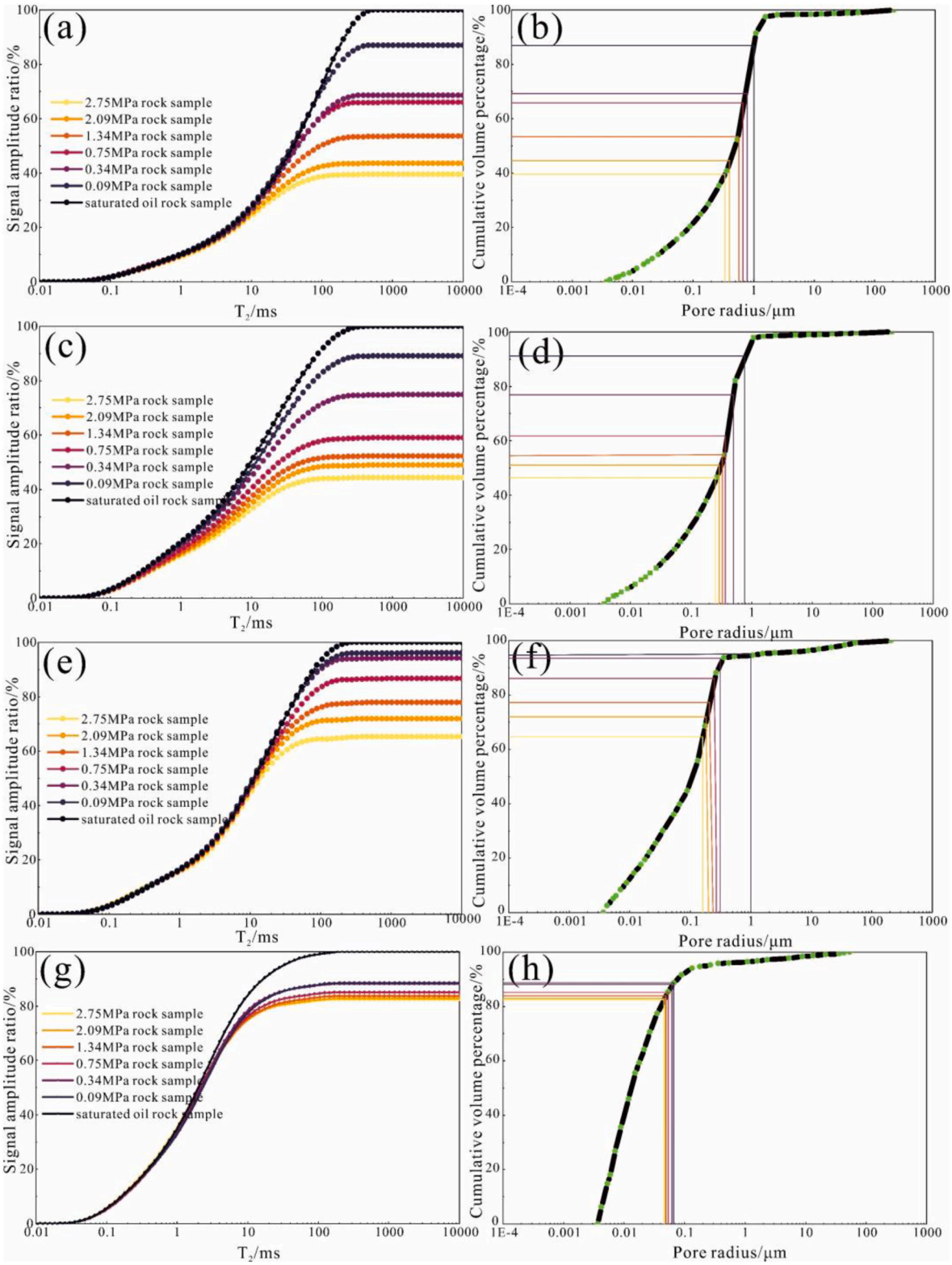


**Fig. 15.** NMR signal accumulation curves and pore cumulative distribution curves at different centrifugal forces in four types of reservoirs. (ăb) Pore structure of DFMS. (c ~ d) Pore structure of DFLS. (e ~ f) Pore structure of STS. (g ~ h) Pore structure of STCS.

cementation dominate, with minor amounts of secondary quartz cementation. Cementation not only plugs primary intergranular pores (Fig. 10e) but also fills secondary feldspar and detrital dissolution pores (Fig. 10f). When the carbonate mineral content exceeds 10%, the rock properties deteriorate sharply, leading to a significant reduction in the MFS (Fig. 10a). Due to the continuous dehydration of the Paleogene $Es_4$ gypsum-salt layer since the Dongying period, the formation water of the third member of the Paleogene Shahejie Formation was alkaline for a period(Wang et al., 2021a,b,c). This exacerbated the cementation of carbonate minerals, especially near the center of the depression where a certain proportion of calcareous fine sandstone (STCS) developed in turbidite facies reservoirs, characterized by poor physical properties and

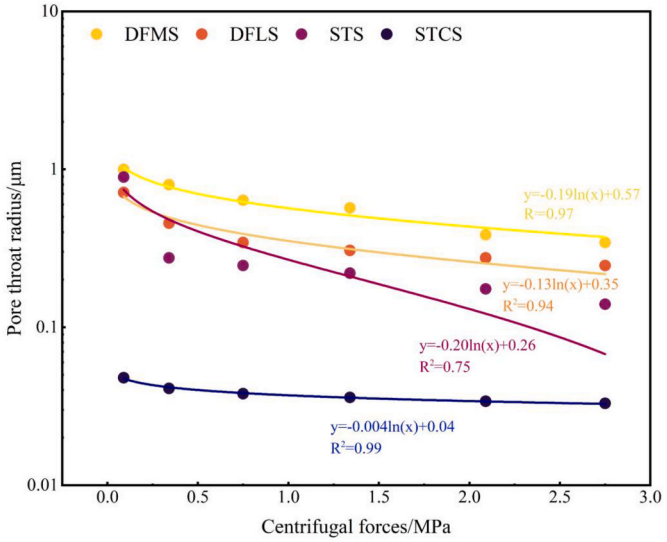


**Fig. 16.** Pore-throat radii of movable fluids under different centrifugal forces in four types of sandstone lithologies.

low MFS (Fig. 11a). Simultaneously, active ion exchange at the sand–mud interface promoted the diffusion of $CO_3^{2-}$, $Fe^{2+}$, $Ca^{2+}$, and $Mg^{2+}$ from mudstone to sandstone, replacing K+ in sandstone and leading to carbonate cementation. The statistical analysis indicated that sandstones farther from the sand–mud interface had lower carbonate mineral contents (Fig. 11b). The influence of clay cementation on fluid mobility is reflected in the different crystal forms and occurrences of various clay components in the reservoir. SEM images show that illite appears in sheet or flocculent forms filling feldspar dissolution pores and intergranular pores between clastic particles (Fig. 4m), resulting in a decrease in reservoir movable fluid saturation (Fig. 12g). In contrast, kaolinite fills feldspar and lithic dissolution pores in a book-like form (Fig. 4i). However, since high kaolinite content often indicates significant feldspar dissolution pores, kaolinite has a weak positive impact on reservoir movable fluid saturation (Fig. 12h). Compared to the other two clay minerals, the content of illite-smectite mixed layers and chlorite has a smaller impact on reservoir movable fluid saturation (Fig. 12f and i). Although secondary porosity can be generated during the kaolinization of feldspar minerals, the strong hydrophilicity of illite and kaolinite makes reservoir fluids prone to strong adsorption, restricting fluid flow. Moreover, illite swells easily upon water absorption, reducing its pore and throat sizes and leading to a decrease in fluid mobility (Hou et al., 2021, Fig. 12c).

Erosion is the main process for creating secondary pores.The Shahejie Formation hydrocarbon source rocks in the Minghuazheng, Guantao (14.0–2.8 MPa), and Dongying (26.2–24.6 MPa) periods underwent two phases of hydrocarbon generation (Li et al., 2023b), resulting in the abundant generation of organic acids. During the transformation process from kaolinite to illite, the amount of acidic pore water increased. Feldspars, lithic fragments, quartz, and carbonate cements were directly eroded to varying degrees, forming intergranular dissolution pores (Fig. 10g and h) and intercrystalline dissolution pores (Fig. 4n). Simultaneously, clastic particles initially altered by carbonate minerals further eroded due to the dissolution of the altering agents in later stages. Erosion processes often initiated along the edges of particles or at structurally weak positions, such as mineral cleavages, forming secondary enlarged intergranular pores and intragrain dissolution pores. Additionally, a partial clay matrix and cement dissolution further enhanced erosion, promoting the improvement of physical properties (Herlinger et al., 2017). An increase in the feldspar and quartz mineral contents is correlated with a significant increase in the MFS, which is also supported by relevant data (Fig. 12d and e).

#### 5.1.2. *Microscopic control of fluid mobility by reservoir pore permeability properties and pore structure*

Differences in sedimentary environments and diagenetic processes during burial result in variations in the petrophysical properties and pore structures of different lithofacies. Parameters such as porosity, pore radius, displacement pressure, and mercury saturation are crucial microscopic geological elements that constrain fluid flow capabilities (Wang et al., 2021b). For tight sandstones, the MFS has a positive correlation with porosity and permeability, with $R^2$ of 0.81 and 0.61, respectively (Fig. 13a and b). Some high-porosity samples deviate from the baseline of the fitted curve, indicating that high porosity does not necessarily represent good pore connectivity. The introduction of the reservoir quality index (RQI) reflects changes in reservoir pore structures. When the RQI is less than 0.22 and the MFS is less than 40% overall (Fig. 13a and b), poor reservoir quality restricts fluid flow.By establishing the correlation between average pore throat radius, movable fluid saturation, and the Reservoir Quality Index (RQI) (Fig. 13c and d), the results show that both MFS and average pore throat radius have a strong positive correlation with the RQI. This indicates that the greater the RQI, the better the reservoir's storage and mobility properties.

The HPMI experiment indicate that the MFS and pore radius are significantly correlated (Fig. 14a). STS and STCS developed in a weak alkaline environment during the Dongying Depression period, with thin-layer sandstone nested in thick mudstone. The proximity of sandstone to the sand–mud interface and active ion exchange favor the occurrence of carbonate cementation. Cementitious materials block residual intergranular and dissolved pores, resulting in smaller pore radii in both deltaic and turbidite sandstones compared to DFMS and DFLS sandstones. The inferior pore structure increases the resistance to fluid injection into the reservoir, as observed in the mercury injection experiment, where an increase in reservoir displacement pressure and a decrease in maximum mercury saturation occur. In production, STS and STCS exhibit poor oil and gas availability, low oil saturation, and low single-well productivity due to their less favorable pore structure (Fig. 14b and c).

### 5.2. *Lower limit of movable fluid pore radius*

This paper performs normalization on the amplitude of $T_2$ spectral signals of oil-saturated samples and plots the cumulative distribution curves under different centrifugal forces (Fig. 15a–c, e, and g). The $T_2$ spectral curves are then horizontally extended to the right, drawing horizontal lines that represent the residual oil signals at corresponding centrifugal forces. These horizontal lines are overlaid on the normalized cumulative distribution curves of HPMI pores (Fig. 15b–d, e, and f). The data at the intersection points on the horizontal axis indicate the minimum pore throat radius required to mobilize reservoir oil under the respective centrifugal forces (Fig. 15b–d, e, f).

An increase in the centrifugal force leads to an exponential decrease in the lower limit of movable fluid pore radius (LLMPR) (Fig. 16). When the centrifugal force reaches 2.09–2.75 MPa, there is a minimal increase in the amount of mobile fluid within the pores, and the NMR signals cease to increase or show only weak increases. This indicates that the NMR experiment has reached the optimal centrifugal force, obtaining the maximum value of mobile fluid saturation under ideal conditions. It is observed that, compared with larger pores, smaller pores require significantly greater centrifugal forces for displacing fluids. At the maximum centrifugal force of 2.75 MPa, the for DFLS, DFMS, STS, and STCS are 0.344, 0.246, 0.140 and 0.033 μm, respectively. Delta front sand bodies require relatively low centrifugal forces to yield a substantial amount of mobile fluid, while turbidite sandstone exhibits a complex pore structure with a greater proportion of micropores. The absence of mesopores and macropores in turbidite sandstone necessitates stronger centrifugal forces to obtain a limited amount of mobile fluid. Considering the ease of recovering oil from larger pores and

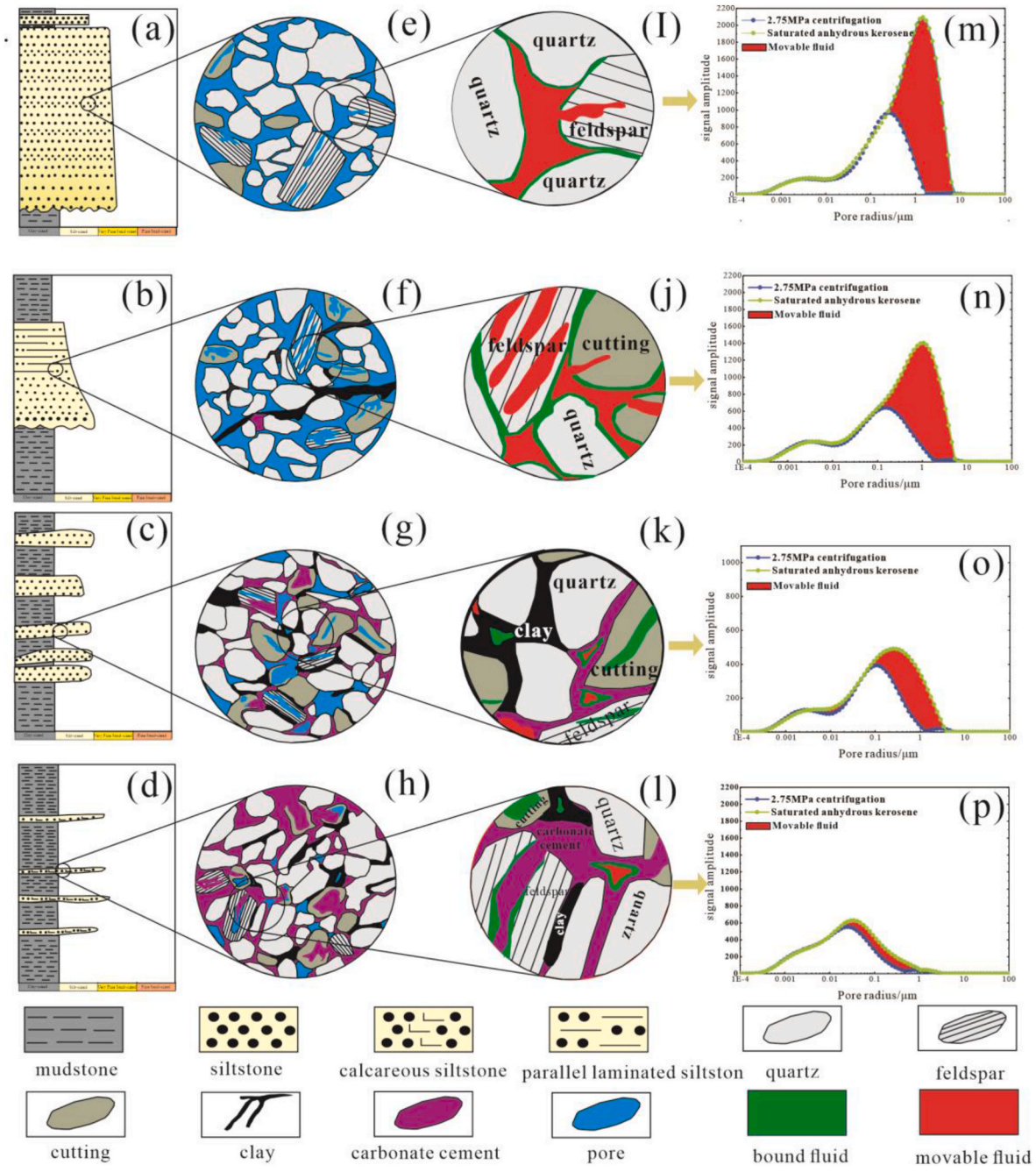


**Fig. 17.** Linnan depression fluid mobility patterns in different sandstone lithofacies. (ād) lacustrine delta-turbidite sandstone lithofacies models. (e ~ h) models of pore networks in four sandstone lithofacies. (i ~ l) models of fluid distribution states in four sandstone lithofacies. (m ~ p) NMR $T_2$ spectra of fluid mobility in four sandstone lithofacies.

microfractures during production, setting the LLMPR at 0.033 μm for deep-seated tight sandstones in the Linnan Depression seems reasonable.

### 5.3. *Differential fluid mobility patterns in the Linnan Depression delta–turbidite-phase sandstones*

In the Linnan Depression, tight sandstones are constrained by macroscopic depositional environments, diagenetic processes, and microscopic storage and permeability characteristics. The four types of sandstones exhibit significant differences in fluid saturation and in the LLMPR under different centrifugal forces. Based on this, a fluid mobility assessment model for the four types of sandstones in the lacustrine delta–turbidite depositional system of the study area is established (Fig. 17). Among them, the blocky sandstone on the delta front (DFMS) has the optimal pore structure and fluid mobility. This lithofacies consists of thick-bedded sandstones with continuous stacking (Fig. 17a) that exhibit strong dynamic water conditions, good mineral particle selectivity, and weak influence from the muddy matrix and carbonate cement (Fig. 17b). The original intergranular and intergranular dissolution pores are well developed and include mesopores and macropores, resulting in the highest fluid mobility. The laminated sandstone on the delta front (MFLS) formed in a weaker dynamic water environment, and the development of muddy bedding affected the original pore spaces (Fig. 17f). However, it still predominantly contains mesopores, ensuring good pore connectivity and permeability, leading to higher fluid saturation (Fig. 17j–n). In contrast, the sandstone lithofacies of the turbidite

depositional system are closer to the center of the basin, with thin single sand bodies and thin layers embedded in thick mudstone (Fig. 17c and d). Under the influence of differential sorting and strong ion exchange at the source–reservoir interface, there are high contents of carbonate cement and mud (Fig. 17g–and h). Most of the intergranular dissolution and original intergranular pores are filled with cement, resulting in poor pore connectivity and low permeability (Fig. 17k and L). Fluids are mostly confined to micropores, leading to poor reservoir mobility (Fig. 17o and p).

## 6. Conclusion

The Paleogene $Es_3$ section of the Linnan Depression contains significant tight oil resources within its lacustrine delta-turbidite facies sandstone deposits. Based on core descriptions, this study identified four lithofacies of sand bodies. We determined the MFS and LLMPR values for these lithofacies using a combination of NMR and centrifugation technique. Factors influencing fluid mobility were analyzed by integrating data from XRD, gas-measured poroperm analysis, microscopic observations, and HPMI, leading to the development of a fluid mobility evaluation model for the lacustrine delta front-turbidite facies sand bodies. The main findings and conclusions are as follows.

(1) In the lacustrine environment, four lithofacies have developed: DFMS, DFLS, STS, and STCS, all comprising lithic feldspathic sandstones and feldspathic sandstones. The DFMS and DFLS lithofacies exhibit more developed primary intergranular and intragranular dissolution pores. In contrast, the STS and STCS lithofacies are characterized by secondary intragranular dissolution pores and intercrystalline pores of clay minerals, resulting in poorer pore connectivity and oil-bearing properties.
(2) Four lithofacies correspond to four types of HPMI pore structures. In DFMS, DFLS, STS, and STCS, the average pore diameter, maximum mercury intrusion saturation, and MFS sequentially decrease, while displacement pressure progressively increases. In DFMS and DFLS, fluids are stored in mesopores and macropores, with mesopores primarily contributing to fluid mobility. In STS and STCS, fluids are confined to micropores and a limited number of mesopores, with micropores making the most significant contribution to fluid mobility.
(3) Provenance, depositional environment, and diagenesis macroscopically affect the fluid mobility of the four lithofacies. Microscopically, reservoir quality and pore structure significantly influence the saturation of movable fluids, with parameters such as RQI, displacement pressure, and average pore diameter playing dominant roles. At the optimal centrifugal force of 2.75 MPa, the LLMPR in the Linnan Depression is calculated to be 0.033 μm.
(4) DFMS and DFLS are the optimal lithofacies for movable fluids, possessing the best pore structure and the highest movable fluid saturation. STS and STCS typically consist of thin sand bodies embedded within thick mudstones, influenced by carbonate cementation and muddy infilling, resulting in poor fluid mobility, and are considered secondary lithofacies. The established fluid mobility model for lacustrine tight sandstones provides a theoretical reference for exploration and effective development in similar geological settings.

## CRediT authorship contribution statement

**Yuchao Wang:** Writing – review & editing, Writing – original draft, Methodology, Investigation, Data curation, Conceptualization. **Dongxia Chen:** Writing – review & editing, Formal analysis, Data curation. **Lanxi Rong:** Investigation, Formal analysis. **Jialing Chen:** Investigation, Formal analysis. **Fuwei Wang:** Methodology, Conceptualization. **Shijie He:** Methodology, Investigation. **Yuqi Wang:** Investigation, Formal analysis. **Zijie Yang:** Investigation, Conceptualization. **Wenzhi Lei:** Investigation.

## Declaration of competing interest

The authors declare that they have no known competing financial interests or personal relationships that could have appeared to influence the work reported in this paper.

## Data availability

The data that has been used is confidential.

## Acknowledgements

This research sincerely acknowledge the financial support from the National Natural Science Foundation of China (Grant No. 41972124).

## References

Alvarado, V., Manrique, E., 2010. Enhanced oil recovery: an update review. 3 (9), 1529–1575. https://doi.org/10.3390/en3091529.
Amaefule, J.O., Altunbay, M., Tiab, D., Kersey, D.G., Keelan, D.K., 1993. Enhanced reservoir description: using core and log data to identify hydraulic (flow) units and predict permeability in uncored intervals/wells. SPE Annual Technical Conference and Exhibition 11, 205–220. https://doi.org/10.2118/26436-MS. Houston, Texas.
Becker, E.D., 1993. A brief history of nuclear magnetic resonance. Analytical chemistry 65 (6), 295A–302A. https://doi.org/10.1021/ac00054a716.
Bjørlykke, K., 2014. Relationships between depositional environments, burial history and rock properties. Some principal aspects of diagenetic process in sedimentary basins. Sediment. Geol. 301, 1–14. https://doi.org/10.1016/j.sedgeo.2013.12.002.
Chukwuma, K., Bordy, E.M., Coetzer, A., 2018. Evolution of porosity and pore geometry in the Permian Whitehill Formation of South Africa–A FE-SEM image analysis study. Mar. Petrol. Geol. 91, 262–278. https://doi.org/10.1016/j.marpetgeo.2017.12.026.
Dai, Q.Q., Wang, G.W., Lu, C.J., Zhang, Y.Z., Zhou, Z.L., Fan, X.Q., Wang, S., He, Z.B., 2018. Occurrence characteristics and controls over mobile fluids in a tight sandstone reservoir. Aust. J. Earth Sci. 65 (6), 877–887. https://doi.org/10.1080/08120099.2018.1491012.
Dong, X.X., Meng, X.Z., Pu, R.H., 2023. Impacts of mineralogy and pore throat structure on the movable fluid of tight sandstone gas reservoirs in coal measure strata: a case study of the Shanxi formation along the southeastern margin of the Ordos Basin. J. Petrol. Sci. Eng. 220, 111257 https://doi.org/10.1016/j.petrol.2022.111257.
Feng, D.X., Ye, F., 2018. Structure kinematics of a transtensional basin: an example from the linnan subsag, Bohai Bay Basin, eastern China. Geosci. Front. 9 (3), 917–929. https://doi.org/10.1016/j.gsf.2017.05.012.
Gao, H., Li, H.Z., 2016. Pore structure characterization, permeability evaluation and enhanced gas recovery techniques of tight gas sandstones. J. Nat. Gas Sci. Eng. 28, 536–747. https://doi.org/10.1016/j.jngse.2015.12.018.
Gao, Z.Y., Duan, L.F., Hu, Q.H., Xiong, S.L., Zhang, T.W., 2021. Effect of shale sample particle size on pore structure obtained from high pressure mercury intrusion porosimetry. Geofluids 2021, 1–15. https://doi.org/10.1155/2021/5581541.
Ge, X.M., Fan, Y.R., Zhu, X.J., Chen, Y.G., Li, R.Z., 2015. Determination of nuclear magnetic resonance T2 cutoff value based on multifractal theory—an application in sandstone with complex pore structure. Geophysics 80 (1), D11–D21. https://doi.org/10.1190/geo2014-0140.1.
Griesinger, C., Bennati, M., Vieth, H.M., Luchinat, C., Parigi, G., Höfer, P., Engelke, f., Glaser, S.J., Denysenkov, V., Prisner, T.F., 2012. Dynamic nuclear polarization at high magnetic fields in liquids. Prog. Nucl. Magn. Reson. Spectrosc. 64, 4–28. https://doi.org/10.1016/j.pnmrs.2011.10.002.
Guo, J.C., Zhou, H.Y., Zeng, J., Wang, K.J., Lai, J., Liu, Y.X., 2020. Advances in low-field nuclear magnetic resonance (NMR) technologies applied for characterization of pore space inside rocks: a critical review. Petrol. Sci. 17, 1281–1297. https://doi.org/10.1007/s12182-020-00488-0.
Guo, Q., Dong, M.C., Mao, H.B., Ju, J.T., 2022. Micro-scale pore-throat heterogeneity of tight oil sandstone reservoirs and its influence on fluid occurrence state. Front. Earth Sci. 10, 959796 https://doi.org/10.3389/feart.2022.959796.
Hachem, D., Sanders, A., Nguyen, Q.P., 2022. Wettability alteration using silane to improve water-alternating-gas injectivity. ACS Omega 7 (43), 39258–39267. https://doi.org/10.1021/acsomega.2c05313.
Han, C.C., Qi, M., Ma, C.F., Zhao, L.Q., Lei, L.Q., Kong, W.T., Li, Z.p., Li, J., Lv, N., Cao, X., 2023. Determination of the lower limit of physical properties of tight oil reservoirs: a case study of the lower E s 3 in the jiangjiadian area, linnan sag. ACS Omega 8 (39), 35856–35865. https://doi.org/10.1021/acsomega.3c03379.
Herlinger Jr, R., Zambonato, E.E., De Ros, L.F., 2017. Influence of diagenesis on the quality of Lower Cretaceous pre-salt lacustrine carbonate reservoirs from northern Campos Basin, offshore Brazil. J. Sediment. Res. 87 (12), 1285–1313. https://doi.org/10.2110/jsr.2017.70.
Hou, C.H., Yu, B.S., Liu, L., Xu, Y.R., Zhang, Y.F., Zhang, L.H., Zhao, J.L., Zhao, X., Zuo, Q.W., Sun, M.D., 2021. Water uptake behavior and influence factors of Longmaxi shale: implications from water physisorption and imbibition

measurements. Energy & Fuels 35 (15), 11958–11975. https://doi.org/10.1021/acs.energyfuels.1c01413.
Hu, S.Y., Zhao, W.Z., Hou, L.H., Yang, Z., Zhu, R.L., Wu, S.T., Bai, B., Jin, X., 2020. Development potential and technical strategy of continental shale oil in China. Petrol. Explor. Dev. 47 (4), 877–887. https://doi.org/10.1016/S1876-3804(20)60103-3.
Jia, C.Z., Pang, X.Q., Song, Y., 2023. Whole petroleum system and ordered distribution pattern of conventional and unconventional oil and gas reservoirs. Petrol. Sci. 20 (1), 1–19. https://doi.org/10.1016/j.petsci.2022.12.012.
Jia, C.Z., Zhang, M., Zhang, Y.F., 2012. Unconventional hydrocarbon resources in China and the prospect of exploration and development. Petrol. Explor. Dev. 39 (2), 139–146. https://doi.org/10.1016/S1876-3804(12)60026-3.
Jiang, M.L., Fang, H.X., Liu, Y., Zhang, Y.F., Wang, C.Q., 2023. On movable fluid saturation of tight sandstone and main controlling factors—case study on the Fuyu oil layer in the Da'an oilfield in the Songliao basin. Energy 267, 126476. https://doi.org/10.1016/j.energy.2022.126476.
Jiang, Y., Xu, G.Q., Bi, H., Shi, Y., Gao, Y., Han, X.L., Zeng, X.H., 2021. A new method to determine surface relaxivity of tight sandstone cores based on LF-NMR and high-speed centrifugation measurements. J. Petrol. Sci. Eng. 196, 108096 https://doi.org/10.1016/j.petrol.2020.108096.
Jiao, L., Andersen, P.Ø., Zhou, J.P., Cai, J.C., 2020. Applications of mercury intrusion capillary pressure for pore structures: a review. Capillarity 3 (4), 62–74. https://doi.org/10.46690/capi.2020.04.02.
Kazemzadeh, E., Ahmadi Shadmehri, M.T., Ebrahimi Salari, T., Salehnia, N., Pooya, A., 2023. Modeling and forecasting United States oil production along with the social cost of carbon: conventional and unconventional oil. Int. J. Energy Sect. Manag. 17 (2), 288–309. https://doi/10.1108/IJESM-02-2022-0010.
Kashefi, K., Pereira, L.C., Chapoy, A., Burgass, R., Tohidi, B., 2016. Measurement and modelling of interfacial tension in methane/water and methane/brine systems at reservoir conditions. Fluid Phase Equil. 409, 301–311. https://doi.org/10.1016/j.fluid.2015.09.050.
Keshavarz, V., Khosravanian, R., Taheri-Shakib, J., Salimidelshad, Y., Hosseini, S.A., 2019. Chemical removal of organic precipitates deposition from porous media: characterizing adsorption and surface properties. J. Petrol. Sci. Eng. 175, 200–214. https://doi.org/10.1016/j.petrol.2018.12.021.
Korb, J.P., 2018. Multiscale nuclear magnetic relaxation dispersion of complex liquids in bulk and confinement. Prog. Nucl. Magn. Reson. Spectrosc. 104, 12–55. https://doi.org/10.1016/j.pnmrs.2017.11.001.
Lai, J., Wang, G.W., Wang, Z.Y., Chen, J., Pang, X.Q., Wang, S.C., Zhou, Z.L., He, Z.B., Qin, Z.Q., Fan, X.Q., 2018. A review on pore structure characterization in tight sandstones. Earth Sci. Rev. 177, 436–457. https://doi.org/10.1016/j.earscirev.2017.12.003.
Li, C., Zhang, L.K., Luo, X.R., Wang, B., Lei, Y.H., Cheng, M., Luo, H.M., Wang, C.J., Yu, L., 2022. Modeling of overpressure generation–evolution of the paleogene source rock and implications for the linnan sag, eastern China. Front. Earth Sci. 10, 829322 https://doi.org/10.3389/feart.2022.829322.
Li, J.D., Li, X.Q., Shi, B.H., Xiang, J., Zhao, Y.F., Sun, D.Y., Tian, W., 2023a. Pore-throat combination characteristics and their effect on gas–water seepage behavior in tight sandstone gas reservoirs of the dingbian area, Ordos Basin, North China. Energy & Fuels 37 (14), 10444–10465. https://doi.org/10.1021/acs.energyfuels.3c01594.
Li, J.L., Wang, X., Wang, W.Q., Li, B., Zeng, J.H., Jia, K.K., Qiao, J.C., Wang, K.T., 2023b. Characteristics of sand-mud structure development in tight sandstone and its control on reservoir space: a case study of the lower sub-member of the third member of Shahejie Formation in Linnan Sag, Bohai Bay Basin. Petroleum and Natural Gas Geology 44 (5), 1173–1187. https://doi.org/10.11743/ogg20230508.
Li, Q., Jiang, Z.X., Liu, K.Y., Zhang, C.M., You, X.L., 2014. Factors controlling reservoir properties and hydrocarbon accumulation of lacustrine deep-water turbidites in the Huimin Depression, Bohai Bay Basin, East China. Mar. Petrol. Geol. 57, 327–344. https://doi.org/10.1016/j.marpetgeo.2014.06.007.
Liu, B., Yan, M., Sun, X.D., Bai, Y.F., Bai, L.H., Fu, X.F., 2020. Microscopic and fractal characterization of organic matter within lacustrine shale reservoirs in the first member of Cretaceous Qingshankou Formation, Songliao Basin, Northeast China. Journal of Earth Science 31, 1241–1250. https://doi.org/10.1007/S12583-020-1345-3.
Liu, H.M., Zhang, S., Song, G.Q., Wang, X.J., Teng, J.B., Wang, M., Bao, Y.S., Yao, S.P., Wang, W.Q., Zhang, S.P., Hu, Q.H., Fan, Z.W., 2019. Effect of shale diagenesis on pores and storage capacity in the paleogene Shahejie Formation, dongying depression, Bohai Bay Basin, east China. Mar. Petrol. Geol. 103, 738–752. https://doi.org/10.1016/j.marpetgeo.2019.01.002.
Liu, M., Xie, R.H., Guo, J.F., Jin, G.W., 2018. Characterization of pore structures of tight sandstone reservoirs by multifractal analysis of the NMR T 2 distribution. Energy & Fuels 32 (12), 12218–12230. https://doi.org/10.1021/acs.energyfuels.8b02869.
Liu, T.S., Ding, W.L., Zhang, R.F., Li, J.T., Feng, G.Y., Han, P.Y., Zhou, X., Ye, D.S., Zhang, Z.Y., 2023. Cenozoic tectonostratigraphy and structural styles in the Nangong Sag, Bohai Bay Basin, eastern China: implications for the generation of oil-gas traps. Mar. Petrol. Geol. 149, 106081 https://doi.org/10.1016/j.marpetgeo.2022.106081.
Ma, L.C., Song, M.S., Wang, Y.S., Wang, Y.G., Liu, H.M., 2023. Exploration progress of the paleogene in Jiyang depression, Bohai Bay Basin. Energy Geoscience 4 (1), 42–50. https://doi.org/10.1016/j.engeos.2022.07.004.
Matthews, G.P., Moss, A.K., Ridgway, C.J., 1995. The effects of correlated networks on mercury intrusion simulations and permeabilities of sandstone and other porous media. Powder Technol. 83 (1), 61–77. https://doi.org/10.1016/0032-5910(94)02942-H.
Meng, Z.Y., Sun, W., Liu, Y.Q., Luo, B., Zhao, M.R., 2021. Effect of pore networks on the properties of movable fluids in tight sandstones from the perspective of multi-techniques. J. Petrol. Sci. Eng. 201, 108449 https://doi.org/10.1016/j.petrol.2021.108449.
Noack, F., 1971. Nuclear magnetic relaxation spectroscopy. In: NMR: Basic Principles and Progress Grundlagen und Fortschritte. Springer Berlin Heidelberg, Berlin, Heidelberg, pp. 83–144.
Pawloski, G.A., 1985. Quantitative determination of mineral content of geological samples by X-ray diffraction. Am. Mineral. 70 (7–8), 663–667.
Pei, L.X., Gang, W.Z., Wang, D.M., Xiong, M., 2017. Application of biomarkers to petroleum migration in the linyi fault area, Huimin depression, Bohai Bay Basin, China. Can. J. Earth Sci. 54 (3), 311–321. https://doi.org/10.1139/cjes-2016-0042.
Qu, Y.Q., Sun, W., Wu, H.N., Huang, S.J., Li, T., Ren, D.Z., Chen, B., 2022. Impacts of pore-throat spaces on movable fluid: implications for understanding the tight oil exploitation process. Mar. Petrol. Geol. 137, 105509 https://doi.org/10.1016/j.marpetgeo.2021.105509.
Rudszuck, T., Förster, E., Nirschl, H., Guthausen, G., 2019. Low-field NMR for quality control on oils. Magn. Reson. Chem. 57 (10), 777–793. https://doi.org/10.1002/mrc.4856.
Slijkerman, W.J., Hofman, J.P., Looyestijn, W., 2001. A practical approach to obtain primary drainage capillary pressure curves from NMR core and log data. Petrophysics-The SPWLA Journal of Formation Evaluation and Reservoir Description 42 (4), 334–343.
Wang, D., Wu, Z.P., Yang, L.L., Liu, H., Zhang, Y., 2020a. Growth and linkage of the Xiakou fault in the linnan sag, Jiyang depression, eastern China: formation mechanism and sedimentation response. Mar. Petrol. Geol. 116, 104319 https://doi.org/10.1016/j.marpetgeo.2020.104319.
Wang, F.W., Chen, D.X., Wang, Q.C., Shi, X.B., Xie, G.J., Wang, Z.Y., Li, J.H., Liao, W.H., 2020b. Evolution characteristics of transtensional faults and their impacts on hydrocarbon migration and accumulation: a case study from the Huimin Depression, Bohai Bay Basin, eastern China. Mar. Petrol. Geol. 120, 104507 https://doi.org/10.1016/j.marpetgeo.2020.104507.
Wang, J.Y., Jiang, F.J., Zhang, C.L., Song, Z.Z., Mo, W.L., 2021a. Study on the pore structure and fractal dimension of tight sandstone in coal measures. Energy & Fuels 35 (5), 3887–3898. https://doi.org/10.1021/acs.energyfuels.0c03991.
Wang, L., Zhao, N., Sima, L.Q., Meng, F., Guo, Y.H., 2018. Pore structure characterization of the tight reservoir: systematic integration of mercury injection and nuclear magnetic resonance. Energy & Fuels 32 (7), 7471–7484. https://doi.org/10.1021/acs.energyfuels.8b01369.
Wang, M., Guo, Z.Q., Jiao, C.X., Lu, S.F., Li, J.B., Xue, H.T., Li, J.J., Li, J.Q., Chen, G.H., 2019. Exploration progress and geochemical features of lacustrine shale oils in China. J. Petrol. Sci. Eng. 178, 975–986. https://doi.org/10.1016/j.petrol.2019.04.029.
Wang, X.L., Zhang, G.S., Tang, W., Wang, D.H., Wang, K., Liu, J.Y., Du, D., 2022. A review of commercial development of continental shale oil in China. Energy Geoscience 3 (3), 282–289. https://doi.org/10.1016/j.engeos.2022.03.006.
Wang, Y.S., Chen, T., Zhang, P.F., Zhai, Z., 2021b. Exploration potential and direction of Palaeogene light crude oil reservoirs in Jiyang depression. Acta Pet. Sin. 42 (12), 1605. https://doi.org/10.7623/syxb202112006.
Wang, Y.Z., Mao, C., Li, Q., Jin, W., Zhu, S.M., Wang, X.D., Wang, Z.G., He, J.Y., Sheng, J.G., Zhu, Y.P., Wang, Y., Wang, H.Y., Tan, B.D., Ren, J.H., 2021c. Pore throat characteristics of tight reservoirs by a combined mercury method: a case study of the member 2 of Xujiahe formation in Yingshan gasfield, North Sichuan Basin. Open Geosci. 13 (1), 1174–1186. https://doi.org/10.1515/geo-2020-0273.
Wang, Z.J., Li, S.Y., Jin, Z.J., Li, Z.M., Liu, Q.Y., Zhang, K.Q., 2023a. Oil and gas pathway to net-zero: review and outlook. Energy Strategy Rev. 45, 101048 https://doi.org/10.1016/j.esr.2022.101048.
Wang, Z.Y., Liu, Y.C., Lu, S.F., Lin, L.M., Zhou, N.W., Liu, Y., 2023b. Differential development characteristics of secondary pores and effects on pore structure and movable fluid distribution in tight gas sandstones in the lower Permian, northeastern Ordos Basin, China. Geoenergy Science and Engineering 224, 211580. https://doi.org/10.1016/j.geoen.2023.211580.
Washburn, K.E., 2014. Relaxation Mechanisms and Shales Concepts Magn.
Wei, Q.L., Zhang, H.F., Han, Y.L., Guo, W.J., Xiao, L., 2023. Microscopic pore structure characteristics and fluid mobility in tight reservoirs: a case study of the chang 7 member in the western xin'anbian area of the Ordos Basin, China. Minerals 13 (8), 1063. https://doi.org/10.3390/min13081063.
Wintsch, R.P., Kvale, C.M., 1994. Differential mobility of elements in burial diagenesis of siliciclastic rocks. J. Sediment. Res. 64 (2a), 349–361. https://doi.org/10.1306/D4267D9D-2B26-11D7-8648000102C1865D.
Wu, Y.N., Huang, Y.P., He, Z.T., Hu, Y., Zhao, X.Z., Sun, L.H., Rem, H., Dai, C.L., 2023. Cation-dependent oil–rock interactions in nanopores: insights from core flooding experiments and molecular dynamics simulations. Energy & Fuels 37 (21), 16564–16572. https://doi.org/10.1021/acs.energyfuels.3c03125.
Wu, Y.P., Liu, C.L., Jiang, F.J., Hu, T., Lv, J.H., Zhang, C.X., Guo, X.G., Huang, L.L., Hu, M.L., Huang, R.D., Rizwan, S.A., Zhao, Y., 2022. Geological characteristics and shale oil potential of alkaline lacustrine source rock in Fengcheng Formation of the Mahu Sag, Junggar Basin, Western China. J. Petrol. Sci. Eng. 216, 110823 https://doi.org/10.1016/j.petrol.2022.110823.
Xia, H.F., Wang, L.H., Han, P.H., Cao, R.B., Zhang, S.Q., Sun, X.D., 2021. Microscopic residual oil distribution characteristics and quantitative characterization of producing degree based on core fluorescence analysis technology. Geofluids 1–17. https://doi.org/10.1155/2021/8827721, 2021.
Yang, W., Wang, Q.Y., Wang, Y.H., Jiang, Z.X., Song, Y., Li, Y.H., Liu, D., Zuo, R.S., Gu, X.M., Zhang, F., 2020. Pore characteristic responses to categories of depositional microfacies of delta-lacustrine tight reservoirs in the Upper Triassic Yanchang Formation, Ordos Basin, NW China. Mar. Petrol. Geol. 118, 104423 https://doi.org/10.1016/j.marpetgeo.2020.104423.

Yao, W.J., Chen, Z.H., Hu, T.T., Liang, Z.L., Jia, C.M., Wu, K.Y., Pan, T., Yu, H.T., Dang, Y.F., 2020. Storage space, pore structure, and primary control of igneous rock reservoirs in Chepaizi Bulge, Junggar Basin, western China: significance for oil accumulation. J. Petrol. Sci. Eng. 195, 107836 https://doi.org/10.1016/j.petrol.2020.107836.

Zang, Q.B., Liu, C.L., Awan, R.S., Yang, X.Y., Lu, Z.D., Li, G.X., Wu, Y.P., Feng, D.H., Ran, Y., 2022. Comparison of pore size distribution, heterogeneity and occurrence characteristics of movable fluids of tight oil reservoirs formed in different sedimentary environments: a case study of the Chang 7 member of Ordos Basin, China. Natural Resources Research 31 (1), 415–442. https://doi.org/10.1007/S11053-021-09986-3.

Zhang, F., Jiang, Z.X., Sun, W., Li, Y.H., Zhang, X., Zhu, L., Wen, M., 2019. A multiscale comprehensive study on pore structure of tight sandstone reservoir realized by nuclear magnetic resonance, high pressure mercury injection and constant-rate mercury injection penetration test. Mar. Petrol. Geol. 109, 208–222. https://doi.org/10.1016/j.marpetgeo.2019.06.019.

Zhang, Q.P., Liu, Y.C., Wang, B.T., Ruan, J.F., Yan, N., Chen, H., Wang, Q., Jia, G.W., Wang, R.N., Liu, H., Xue, C.W., Liu, F.L., Yan, H., Zhu, Y.S., 2022. Effects of pore-throat structures on the fluid mobility in chang 7 tight sandstone reservoirs of longdong area, Ordos Basin. Mar. Petrol. Geol. 135, 105407 https://doi.org/10.1016/j.marpetgeo.2021.105407.

Zhao, H.W., Ning, Z.F., Zhao, T.Y., Zhang, R., Wang, Q., 2016. Effects of mineralogy on petrophysical properties and permeability estimation of the Upper Triassic Yanchang tight oil sandstones in Ordos Basin, Northern China. Fuel 186, 328–338. https://doi.org/10.1016/j.fuel.2016.08.096.

Zhao, J.Y., Yang, L., Cai, Y.C., 2021. Combining mercury intrusion porosimetry and fractal theory to determine the porous characteristics of wood. Wood Sci. Technol. 55, 109–124. https://doi.org/10.1007/s00226-020-01243-9.

Zheng, S.J., Yao, Y.B., Liu, D.M., Cai, Y.D., Liu, Y., 2018. Characterizations of full-scale pore size distribution, porosity and permeability of coals: a novel methodology by nuclear magnetic resonance and fractal analysis theory. Int. J. Coal Geol. 196, 148–158. https://doi.org/10.1016/j.coal.2018.07.008.

Zheng, S.J., Yao, Y.B., Liu, D.M., Cai, Y.D., Li, Y., Li, X.W., 2019. Nuclear magnetic resonance T2 cutoffs of coals: a novel method by multifractal analysis theory. Fuel 241, 715–724. https://doi.org/10.1016/j.fuel.2018.12.044.

Zou, C.N., Zhai, G.M., Zhang, G.Y., Wang, H.J., Zhang, G.S., Li, J.Z., Wang, Z.M., Wen, Z. X., Ma, F., Liang, Y.B., Yang, Z., Li, X., Liang, K., 2015. Formation, distribution, potential and prediction of global conventional and unconventional hydrocarbon resources. Petrol. Explor. Dev. 42 (1), 14–28. https://doi.org/10.1016/S1876-3804(15)60002-7.

Zhou, H.W., Jiang, Z.X., Dong, j., Wu, Z.P., L, W., 2013. Study on Fault Activity in Linnan Area of Huimin Depression, Bohai Bay. Adv. Mater. Res. 616, 133–136. https://doi.org/10.4028/WWW.SCIENTIFIC.NET/AMR.616-618.133.